Polarimetric Radar Relations for Estimation of Visibility in Aggregated Snow

PETAR BUKOVČIĆ,[a,b] ALEXANDER V. RYZHKOV,[a,b] AND JACOB T. CARLIN[a,b]

[a] *Cooperative Institute for Mesoscale Meteorological Studies, University of Oklahoma, Norman, Oklahoma*
[b] *NOAA/OAR/National Severe Storms Laboratory, Norman, Oklahoma*

(Manuscript received 19 June 2020, in final form 18 January 2021)

ABSTRACT: The intrinsic uncertainty of radar-based retrievals in snow originates from a large diversity of snow growth habits, densities, and particle size distributions, all of which can make interpreting radar measurements of snow very challenging. The application of polarimetric radar for snow measurements can mitigate some of these issues. In this study, a novel polarimetric method for quantification of the extinction coefficient and visibility in snow, based on the joint use of radar reflectivity at horizontal polarization Z and specific differential phase K_{DP}, is introduced. A large 2D-video-disdrometer snow dataset from central Oklahoma is used to derive a polarimetric bivariate power-law relation for the extinction coefficient, $\sigma_e(K_{DP}, Z) = \gamma K_{DP}^{\alpha} Z^{\beta}$. The relation is derived for particle aspect ratios ranging from 0.5 to 0.8 and the width of the canting angle distribution ranging from 0° to 40°, values typical of aggregated snow, and validated via theoretical and analytical derivations/simulations. The multiplier of the relation is sensitive to variations in particles' densities, the width of the canting angle distribution, and particles' aspect ratios, whereas the relation's exponents are practically invariant to changes in the latter two parameters. This novel approach is applied to polarimetric S-band WSR-88D data and verified against previous studies and in situ measurements of the extinction coefficient for four snow events in the eastern United States. The polarimetric radar estimates of the extinction coefficient exhibit smaller biases in comparison to previous studies concerning the ground measurements. The results indicate that there is good potential for reliable radar estimates of visibility from polarimetric weather radars, a parameter inversely proportional to the extinction coefficient.

KEYWORDS: Snow; Visibility; In situ atmospheric observations; Radars/Radar observations; Remote sensing

1. Introduction

Visibility is a measure of atmospheric opacity. It has an enormous impact on transportation safety in airborne and ground-based traffic, especially in winter weather conditions. Reduced visibility in winter precipitation is one of the major contributing factors in motor vehicle collisions and aircraft crashes. Black and Mote (2015) reported that ~59% of all weather-related fatalities per year (during the 1996–2011 period) were attributed to winter precipitation-related motor vehicle accidents, along with ~1% of aviation accidents. 84% of these motor vehicle crashes were caused by snow, compared to just 16% from ice pellets/freezing rain.

Historically, numerous studies have focused on measuring visibility in snow. These were mostly based on in situ measurements of the extinction (attenuation) of visible light in snow, which is inversely proportional to visibility and associated with the snowfall rate (S). A number of power-law relations between the visibility and S, of the form visibility $= pS^q$, have been proposed (Poljakova and Tretjakov 1960; Lillesæter 1965; Mellor 1966; Warner and Gunn 1969, hereafter WG-69; O'Brien 1970; Bisyarin et al. 1971; Muench and Brown 1977; Fujiyoshi et al. 1983, hereafter FJ-83; Stallabrass 1985; Rasmussen et al. 1999). These relations show a moderate degree of scattering between the visibility/extinction coefficient and S attributable to variability in snowflakes' constituent crystal habits and their degree of riming, aggregation, and wetness, as well as the different methods for determining visibility between day and night (Rasmussen et al. 1999).

With the relative complexity afforded by modern microphysical parameterization schemes used in most operational numerical weather prediction models, the ability to derive operationally useful parameters such as visibility from the model state variables and at all model grid points is desirable. Stoelinga and Warner (1999) proposed a set of parameterizations for visibility based on the mass concentration of several hydrometeor species for use with the Weather Research and Forecasting (WRF) Model. Another example is the Rapid Update Cycle (RUC) model's visibility algorithm, which updated the Stoelinga and Warner (1999) relations and includes an extinction coefficient for graupel (Benjamin et al. 2004). Assuming a gamma particle size distribution, Boudala and Isaac (2009) developed a parameterized relation for the extinction coefficient (and visibility) using temperature and snowfall rate data from aircraft and in situ measurements. Gultepe et al. (2010) utilized both probabilistic and deterministic approaches to develop several parameterizations between visibility and S for use in numerical weather prediction models.

The U.S. National Weather Service (NWS) operationally utilizes the visibility—S relation in an inverse manner by using automatic and/or manual in situ measurements of visibility to estimate S (Interagency Council on Advancing Meteorological Services 2017). For example, the reported surface visibility from Automated Surface Observing System (ASOS) stations is used for snow intensity estimation based on the following criteria: light snow (−SN) if visibility $>$ 1.2 mi; moderate snow (SN) if visibility $>$ 1/4 mi but $\leq$ 1/2 mi; and heavy snow (+SN) if visibility $\leq$ 1/4 mi (1 mi $\approx$ 1.609 km). A similar set of criteria for determining snow intensity is used if visibility is estimated

Corresponding author: Petar Bukovčić, petar.bukovcic@ou.edu

DOI: 10.1175/JTECH-D-20-0088.1

by an observer. An analysis of aircraft accidents caused by ice/snow during takeoff showed that estimates of S from visibility may not be sufficiently accurate for proper aircraft deicing (Rasmussen et al. 1999). Different types of crystals (and snow aggregate constituents) can result in very different visibilities for the same snowfall rate due to their different optical properties, highlighting the tenuous relationship between S and visibility.

Previous studies and current NWS operations are based on a point in situ measurements of extinction coefficient/visibility and do not make use of broad-area remote sensing (e.g., radar) for estimating these parameters. An exception is a study of Muench and Brown (1977), where in situ measurements of extinction coefficient were complemented by a radar-based estimate using the horizontal reflectivity factor Z. These Z-based estimates of the extinction coefficient also exhibited a moderate to a large degree of scattering when compared to in situ measurements.

The polarimetric Next Generation Weather Radar (NEXRAD) network offers immense capabilities for estimating hydrometeor characteristics. In the last three decades, only a few studies have explored quantitative polarimetric snow retrievals, with most focused on ice water content estimation (Vivekanandan et al. 1994; Aydin and Tang 1995; Ryzhkov and Zrnić 1998; Ryzhkov et al. 2018; Lu et al. 2015; Nguyen et al. 2017, 2019). Recently, polarimetric relations for S were proposed for the C band using Z and differential reflectivity Z_{DR} (Hassan et al. 2017), while relations using Z and specific differential phase K_{DP} were proposed at both S (Bukovčić 2017; Bukovčić et al. 2018, 2020) and X (Capozzi et al. 2020) bands. These studies demonstrated that the addition of Z_{DR} (to Z) produces comparable results to Z-based relations, while the addition of K_{DP} enhances the accuracy of snowfall rate estimates concerning the Z-based relations.

In this study, we use an extensive dataset of snow size distributions (SSDs) obtained from a two-dimensional video disdrometer (2DVD) to derive polarimetric bivariate power-law relations for the extinction coefficient and visibility utilizing K_{DP} and Z, following the approach of Bukovčić et al. (2018, 2020). These novel polarimetric relations are applied to four high-impact winter storm cases in the eastern United States that were observed with polarimetric WSR-88Ds to verify the proposed methodology for estimating the extinction coefficient/visibility in dry aggregated snow.

The structure of the paper is as follows. Data sources and processing are described in section 2. Theoretical and empirical considerations of polarimetric estimates of extinction coefficient/visibility are discussed in section 3. Examples of polarimetric radar estimates of extinction coefficient are presented in section 4, followed by a discussion of caveats in section 5 and a summary of results in section 6.

2. Data sources and processing

a. 2DVD data and processing

An extensive 2DVD (Kruger and Krajewski 2002; Schönhuber et al. 2008) snow dataset, obtained in Oklahoma from November 2006 to March 2015, served as the basis for the derivation of polarimetric relations for estimating S and ice water content in Bukovčić et al. (2018, 2020). The same dataset is used here for deriving the extinction coefficient and visibility. The 2DVD is an optical instrument that directly measures particles' size, shape, and terminal velocity, allowing for the construction of particle size distributions. Two (orthogonal) line-scan cameras produce corresponding images of the same particle (with a slight time offset due to a ~6.2–7 mm vertical displacement between the two). The particle is "matched" if the images from both cameras are determined to correspond to the same particle, and "mismatched" if they do not. The true particle terminal velocity and size is determined only if the particle is "matched." Due to snowflake asymmetry, there is a large amount of particle "mismatching" using the manufacturer's proprietary software (Hanesch 1999; Huang et al. 2010, 2015). We have developed and applied a filter to the manufacturer's matching software output to determine the degree of particle matching. The filter utilizes the ratio of particle vertical dimensions (measured from the orthogonal cameras) and the ratio of the measured and empirically predetermined terminal velocity [see Bukovčić et al. (2018) for details]. The product of these ratios, which represents a proxy of particle matching degree, is then used to obtain an adaptable matching threshold. This threshold depends on the measured amount of snow water equivalent (from precipitation gauge) for a particular storm and is used to discard particles with a smaller matching degree.

About 7000 one-minute SSDs were sampled by the 2DVD during 16 snow events. According to the measured temperature and humidity [from in situ observations and RUC or Rapid Refresh (RAP) thermodynamic profiles], the majority of precipitation was classified as dry aggregated snow, whereas mixed-phase precipitation was excluded from the dataset. In 4 of the 16 snow events, short periods of ambient winds exceeding 4 m s^{-1} existed; these were also excluded from further data processing. We adopted the Zhang (2016) approach for determining a proxy for particle density. The Brandes et al. (2007) snow density relation served as the first guess, which was scaled by the square of the measured and prescribed particle terminal velocity ratio as a proxy for the riming factor f_{rim}, where $f_{rim} = 1$ for unrimed snow and $f_{rim} = 5$ for heavily rimed snow (Zawadzki et al. 2005; Brandes et al. 2007). However, the 2DVD-estimated f_{rim} can assume values smaller than 1 if the measured falling velocities are smaller than prescribed. In our 2DVD dataset, the average f_{rim} ranged from 1.23 to 1.6 for individual events, whereas for the entire dataset, the median (mean) f_{rim} was 1.37 (1.40), implying a very light degree of riming. Also, the average SSD was biexponential rather than exponential in form.

b. Radar data and processing

Polarimetric radar measurements contain an abundance of information regarding precipitation processes. However, not all measurements are equally useful without additional processing. Recently introduced radar data displaying/averaging techniques, such as quasi-vertical profiles (QVPs; Ryzhkov et al. 2016; Griffin et al. 2018), range-defined QVPs (RD-QVPs; Tobin and Kumjian 2017), enhanced vertical profiles

TABLE 1. Typical WSR-88D system specifications.

Parameter	Value
Frequency	2700 to 3000 MHz
Transmitter power	700 kW
Average power	300 to 1300 W
Pulse widths	1.57 μs (short) and 4.71 μs (long)
Antenna diameter	8.54 m
Gain at 2850 MHz	45.5 dB
Beamwidth at 2850 MHz	0.925°
Receiver bandwidth	0.63 MHz
System noise power	−113 dBm
Azimuth increment	0.5° and 1°
Range increment	250 m

(EVPs; Bukovčić et al. 2017), columnar vertical profiles (CVPs; Murphy et al. 2020; Bukovčić et al. 2020), and range–height indicator scan-based quasi-vertical profiles (R-QVPs; Allabakash et al. 2019), increase the statistical accuracy of polarimetric variables through additional averaging. This increase in statistical accuracy is important for Z_{DR} and especially K_{DP} in dry (aggregated) snow, which have noisy and very low intrinsic values at S band (e.g., typical values of K_{DP} are near 0.05° km^{-1}). However, several key features make K_{DP} very attractive to use: it is not biased by system noise, attenuation, or radar miscalibration, and compared to Z, it is proportional to a lower-order moment of the SSD. For the aforementioned quasi-vertical profile techniques, 360° azimuthal averaging reduces the standard deviation of the polarimetric variables by a factor of $(360)^{1/2} \approx 19$ (Ryzhkov et al. 2016). This technique improves the statistical accuracy of K_{DP} to greater than 0.01° km^{-1}. Spatial (areal) averaging with a similar number of points produces equally good results. The radar data in this study are obtained from four operational WSR-88D RD-QVPs with a 15-km radius and CVPs (EVPs) with a 10-km (3-km) radius (chosen depending on the radar–ASOS distance) in dry and mostly aggregated snow. Technical details about standard WSR-88Ds are presented in Table 1. The RD-QVPs, EVPs, and CVPs are obtained by azimuthal and/or spatial averaging of the radar measurements utilizing PPI radar scans and displayed as vertical profiles in a time versus height format. RD-QVPs are a radar-centric product whereas CVPs/EVPs are not; CVPs/EVPs can be moved and centered above the point of interest anywhere within the radar domain (in practice up to 90–100 km away from the radar). Hence, in this study, RD-QVPs are used if the ASOS station is very close to the radar location (less than 5–6 km), otherwise, CVPs are utilized; EVPs (i.e., smaller-scale CVPs with a 3-km radius) are applied if the process is spatially localized. All three techniques depict only a proxy of the predominant processes occurring within the designated volume used for their construction and work very well in spatially homogenous precipitation. However, the underlying microphysical processes in heterogeneous precipitation are averaged and sometimes can be difficult to resolve and distinguish.

The relative calibration of reflectivity is not checked because the WSR-88Ds are calibrated to be within 1 dB. The Z_{DR} calibration is performed by comparing the estimated Z_{DR} values (from RD-QVPs/CVPs/EVPs) in dry aggregated snow (relatively close to the ground) with the expected Z_{DR} values of 0.1–0.15 dB. The slope of Φ_{DP} from a 6-km (2-km) range window is used to estimate K_{DP} if $Z < 40$ dBZ ($Z > 40$ dBZ), allowing for relatively reliable estimates of K_{DP} starting at 8–10 km in radial distance from the radar. Hence, more reliable K_{DP} estimates in RD-QVPs start at a height of ~350 m above the radar due to the combined effects of the radar "dead zone" (no data in first 2.125 km for WSR-88D) and K_{DP} processing from the lowest two to four radar elevation angles.

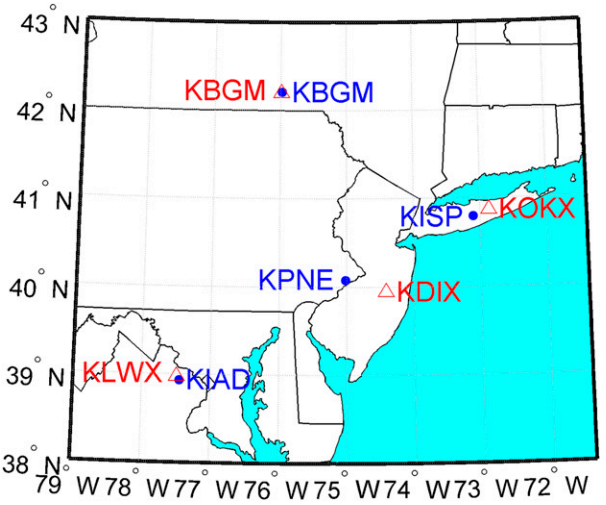

FIG. 1. Map of the northeastern coast of the United States with relative locations of WSR-88D (KLWX, KDIX, KOKX, and KBGM; red triangle markers) and ASOS (KIAD, KPNE, KISP, and KBGM; blue solid dots) sites.

c. *ASOS data and processing*

Measurements of extinction coefficient from ASOS sites are used as a ground reference for the selected events. The values used in this study (and that are reported by ASOS) represent 1-min averages of the observed extinction coefficient from all available sensors (NWS 1998). The time difference between the radar estimates aloft (200–700 m) and the ASOS extinction coefficient sensor(s) is adjusted for an average snowflake terminal velocity (assumed to be 1 m s^{-1}). The relative locations between the WSR-88D and the selected ASOS sites are presented in Fig. 1.

3. Polarimetric relations for extinction coefficient and visibility estimation

a. *Definition of visibility*

In radar terminology, the extinction (or attenuation) coefficient σ_e is the fractional reduction of the power density which comes from plane-wave radiation (per unit pathlength). Visibility, a parameter inversely proportional to the extinction coefficient, is defined as the "greatest distance at which a black object of suitable dimensions can be seen and recognized against the horizon sky during daylight or could be seen and

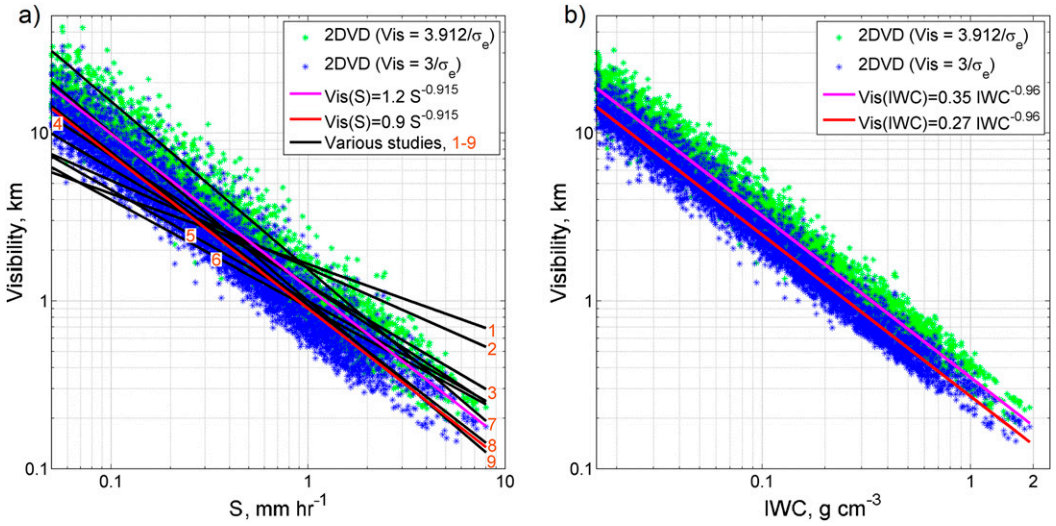

FIG. 2. The dependency of daytime visibility on (a) snowfall rate (S) from 2DVD (blue asterisks: 5%; green asterisks: 2% threshold), polynomial fit from 2DVD data (red curve: 5%; magenta curve: 2% threshold) and various studies from literature (black curves: 1) Poljakova and Tretjakov 1960; 2) Lillesæter 1965; 3) Mellor 1966; 4) WG-69; 5) O'Brien 1970; 6) Bisyarin et al. 1971; 7) Muench and Brown 1977; 8) FJ-83; 9) Stallabrass 1985) and (b) ice water content (IWC) from 2DVD (blue asterisks: 5%; green asterisks: 2% threshold), polynomial fit from 2DVD data (red curve: 5%; magenta curve: 2% threshold).

recognized during the night if the general illumination were raised to the normal daylight level'' (World Meteorological Organization 2003). Hence, the definition of visibility depends on whether it is daytime or nighttime. The relation between σ_e and the visibility during the daytime, Vis_d, is given via the Koschmieder (1924) formula:

$$\mathrm{Vis}_d = -\frac{\ln(\varepsilon)}{\sigma_e}, \tag{1}$$

where ε is the brightness threshold constant, Vis_d is in km, and σ_e is in km^{-1}. The brightness threshold constant is defined as either 2% ($\varepsilon = 0.02$) or 5% ($\varepsilon = 0.05$). The World Meteorological Organization (2008) recommends a 5% brightness threshold for operational usage, which implies a reduction in visibility of about 23% compared to if the 2% threshold is used. The application of a 5% threshold convention to (1) gives

$$\mathrm{Vis}_d = \frac{3}{\sigma_e}. \tag{2}$$

Some previous studies (e.g., Rasmussen et al. 1999) have used the 2% brightness threshold which gives a higher numerator of 3.912 in (2). It is not entirely clear whether 5% or 2% are optimal values for different precipitation conditions.

The dependence of Vis_d on S from various studies (discussed in section 1), along with the 2DVD Oklahoma dataset obtained in dry aggregated snow (using both thresholds of 5% and 2%) are presented in Fig. 2a. Except for two curves (1—Poljakova and Tretjakov 1960; and 2—Lillesæter 1965), the 2DVD estimates of visibility (vs snowfall rate) align very well with the results of previous studies.

Estimating nighttime visibility is more complex than its daytime counterpart because it requires additional parameters beyond σ_e and is governed by Allard's (1876) law. This law was used by Rasmussen et al. (1999) to make a connection between daytime and nighttime visibility. Boudala and Isaac (2009) simplified the Rasmussen et al. (1999) relation, and subsequently, Boudala et al. (2012) derived a simple parameterization between daytime and nighttime visibility as

$$\mathrm{Vis}_n = 1.31 \times \mathrm{Vis}_d^{0.71}, \tag{3}$$

where the subscripts d and n represent day and night. The daytime versus nighttime visibility provides another source of uncertainty for visibility estimates.

b. *Parameterization of the extinction coefficient by S and IWC*

Most previous studies explored and established relations between σ_e/visibility and S (Poljakova and Tretjakov 1960; Lillesæter 1965; Mellor 1966; WG-69; O'Brien 1970; Bisyarin et al. 1971; Muench and Brown 1977; FJ-83; Stallabrass 1985; Rasmussen et al. 1999). The extinction coefficient σ_e (in km^{-1}) is defined as the second moment of the snow size distribution,

$$\sigma_e = \frac{\pi}{2} 10^{-3} \int_0^{D_{\max}} D^2 N(D)\, dD, \tag{4}$$

where D is snowflake equivolume diameter in mm, and $N(D)$ is in $\mathrm{m}^{-3}\,\mathrm{mm}^{-1}$.

Snowfall rate ($\mathrm{mm\,h}^{-1}$),

$$S = 0.6 \times 10^{-3} \pi \int_0^{D_{\max}} \frac{\rho_s(D)}{\rho_w} D^3 V_t(D) N(D)\, dD \tag{5}$$

is also very close to the second SSD moment for low-density (aggregated) snow, where particle density ρ_s (g cm^{-3}) is inversely proportional to particle diameter D (mm),

$$\rho_s(D) = \alpha' D^{\beta_1} = \alpha_1 f_{\rm rim} D^{\beta_1}, \tag{6}$$

and $\beta_1 \approx -1$. Because the fall velocity of snow V_t (m s^{-1}) is a weak function of particle diameter D,

$$V_t(D) = \tau_1 D^{\delta_1} = d_1 f(\rho_a) D^{\delta_1}, \tag{7}$$

where τ_1 and $f(\rho_a)$ are functions of atmospheric density and/or pressure, S is proportional to a slightly higher moment of the SSD than σ_e due to the exponent δ_1 in (7). It can be shown (see the appendix) that the relation between σ_e (km^{-1}) and S (mm h^{-1}) has a functional form

$$\sigma_e = \frac{6.66 \times 4^{\beta_1+\delta_1}}{\alpha_1 f_{\rm rim} d_1 f(\rho_a) \Gamma(4+\beta_1+\delta_1) D_m^{1+\beta_1+\delta_1}} S \tag{8}$$

if an inverse exponential SSD (Gunn and Marshall 1958; Sekhon and Srivastava 1970; Lo and Passarelli 1982; Mitchell et al. 1990; Field and Heymsfield 2003; Matrosov and Heymsfield 2017) of the form

$$N(D) = N_{0s} \exp(-\Lambda_s D), \tag{9}$$

where $N(D)$ is in m^{-3} mm^{-1}, is assumed. Using parameter values characteristic of low-density aggregates (e.g., Brandes et al. 2007), (8) becomes

$$\sigma_e = \frac{6.35}{f_{\rm rim}} \left(\frac{p}{p_0}\right)^{0.5} S D_m^{-0.23} \tag{10}$$

for $\alpha_1 = 0.178$, $\beta_1 = -0.922$, $\delta_1 = 0.15$, $d_1 = 0.81$, and $f(\rho_a) = (p_0/p)^{0.5}$, where $p_0 = 1013$ hPa, and p (hPa) is atmospheric pressure (for a standard atmosphere) at the measurement altitude above mean sea level [see (3) in Bukovčić et al. 2020]. It is seen from (8) and (10) that σ_e is a function of S, but also an inverse function of mean volume diameter D_m and $f_{\rm rim}$, which previous studies did not take into account. This may (partly) be the reason why there is a moderate degree of scattering between σ_e and S in previous studies.

Another microphysical parameter, ice water content IWC, can be used for parameterizing σ_e and is even closer to the second moment of the SSD than S in low-density (aggregated) snow. Starting from a basic equation for IWC (g m^{-3}),

$$\mathrm{IWC} = \frac{\pi}{6} \times 10^{-3} \int_0^{D_{\max}} \rho_s(D) D^3 N(D)\, dD, \tag{11}$$

it can be shown (see the appendix) that the σ_e is linearly related to IWC/$f_{\rm rim}$ as

$$\sigma_e = \frac{3}{\alpha'} \mathrm{IWC} = \frac{16.85}{f_{\rm rim}} \mathrm{IWC} \tag{12}$$

if an exponential SSD (9) is used and $\alpha' = \alpha_1 f_{\rm rim}$ ($\alpha_1 = 0.178$; Brandes et al. 2007).

The 2DVD estimates also confirm that the correlation coefficient between the IWC and visibility is higher (0.98 in linear and 0.99 in logarithmic space) than the one between S and visibility (0.94 in linear and 0.98 in logarithmic space), as seen in Fig. 2b. Polynomial fitting (in logarithmic space) produces an inverse, almost linear dependence of visibility (or, equivalently, σ_e) on IWC, where Vis = 0.27×IWC$^{-0.96}$ (red curve in Fig. 2b) for the 5% threshold or Vis = 0.35×IWC$^{-0.96}$ (magenta curve in Fig. 2b) if the 2% threshold is used. Hence, the empirical relation for the extinction coefficient is σ_e = 11.03×IWC$^{0.96}$. This is close to the theoretical relation (12), which for $\alpha_1 = 0.178$ (Brandes et al. 2007) and $f_{\rm rim} = 1.5$ gives $\sigma_e = 11.24$IWC.

c. *Theoretical polarimetric relation for estimating σ_e*

A theoretical relation for polarimetric estimation of σ_e at S band can be derived in the Rayleigh approximation assuming an exponential SSD (9). The basic formulas for Z (mm^6 m^{-3}) and $K_{\rm DP}$ (° km^{-1}) are

$$Z = \frac{|K_i|^2}{|K_w|^2} \int_0^{D_{\max}} \frac{\rho_s^2(D)}{\rho_i^2} D^6 N(D)\, dD, \tag{13}$$

and

$$K_{\rm DP} = \frac{0.27\pi F_o F_s}{\lambda \rho_i^2} \left(\frac{\varepsilon_i - 1}{\varepsilon_i + 2}\right)^2 \int_0^{D_{\max}} \rho_s^2(D) D^3 N(D)\, dD, \tag{14}$$

where $D_{\max}$ is the maximum particle size, D is the equivolume diameter, $N(D)$ is the snow size distribution, $K_i = (\varepsilon_i - 1)/(\varepsilon_i + 2)$, $K_w = (\varepsilon_w - 1)/(\varepsilon_w + 2)$, ε_i and ε_w are the dielectric constants of solid ice and water, ρ_s and ρ_i are the densities of snow and solid ice, and λ is the radar wavelength. The shape parameters L_a and L_b determine the shape factor $F_s = L_b - L_a$ [see Eq. (18) in Bukovčić et al. 2018], whereas the orientation factor $F_o = (1/2)\exp(-2\sigma^2)[1 + \exp(-2\sigma^2)]$ is determined by the width of the canting angle distribution σ (in radians). Note that σ_e and σ are, respectively, the extinction coefficient and the width of the canting angle distribution in our notation. Combining (4), (9), (13), and (14), the following theoretical (subscript t) relation is derived (see the appendix):

$$\sigma_{et} = \gamma_t K_{\rm DP}^{(4+2\beta_1)/3} Z^{-(1+2\beta_1)/3}, \tag{15}$$

where

$$\gamma_t = \frac{\pi \times 10^{-3} \times [0.2243 \times \Gamma(7+2\beta_1)]^{(1+2\beta_1)/3}}{\alpha_1^2 f_{\rm rim}^2 \times \left[0.1777 \times \frac{F_o F_s}{\lambda} \times \Gamma(4+2\beta_1)\right]^{(4+2\beta_1)/3}}, \tag{16}$$

and Γ is the complete gamma function, λ is a radar wavelength (mm), and the factors F_o and F_s are unknown a priori. It is worth noting that Z is proportional to the fourth moment and $K_{\rm DP}$ to the first moment of the (exponential) SSD (Bukovčić et al. 2018) if the particle diameter is inversely proportional to snow density (i.e., if $\beta_1 \approx -1$; Brandes et al. 2007). Hence, the combination of $K_{\rm DP}$ and Z in Eq. (15) is very close to the second SSD moment and thus σ_e. For example, if $\lambda = 110.8$ mm (S band), $\sigma = 15°$ ($F_o \approx 0.816$), aspect ratio $b/a = 0.6$ ($F_s \approx 0.214$), and $f_{\rm rim} = 1.5$, (15) becomes

$$\sigma_{et} = 8.7 K_{DP}^{0.72} Z^{0.28}. \quad (17)$$

Using the threshold $\varepsilon = 0.05$ (5%), (17), and (1), the theoretical expression for daytime visibility (herein visibility) becomes

$$\mathrm{Vis}_t = 0.345 K_{DP}^{-0.72} Z^{-0.28}, \quad (18)$$

whereas using the threshold $\varepsilon = 0.02$ (2%),

$$\mathrm{Vis}_t = 0.45 K_{DP}^{-0.72} Z^{-0.28}. \quad (19)$$

d. Empirical polarimetric relation for estimating σ_e

The 2DVD dataset described in section 2 (and in Bukovčić et al. 2018) is used to derive an empirical polarimetric relation for σ_e. Here, the polarimetric estimate of σ_e assumes an aspect ratio b/a of 0.6 that is typical of aggregated snow (Korolev and Isaac 2003; Matrosov et al. 2005b; Hogan et al. 2012; Garrett et al. 2015). In addition, a linear increase in σ from the dendritic growth layer (DGL) toward the ground is hypothesized to occur during aggregation. Previous studies (Matrosov et al. 2005a; Melnikov and Straka 2013) support this assumption; σ is close to 10° within the DGL ($-20° < T_{air} < -10°$C), while at higher temperatures below the DGL and during more intense aggregation, σ can extend up to 40° (Hendry et al. 1987). The latter finding is also supported by Garrett et al. (2015), who found that particle canting is likely determined by short-term interactions with ambient air, with turbulence acting to increase σ. Using the same Oklahoma 2DVD dataset and a similar approach as in Bukovčić et al. (2020) (i.e., varying the range of b/a from 0.5 to 0.8 and σ from 0° to 40°), a polarimetric relation for estimating σ_e, $\sigma_e(K_{DP}, Z)$, is obtained:

$$\sigma_e(K_{DP}, Z) = \frac{139.9 \times 10^{-3}}{(F_o F_s)^{0.634}} (K_{DP}\lambda)^{0.634} Z^{0.258}. \quad (20)$$

Equation (20) is reduced to $\sigma_e(K_{DP}, Z) = 8.37 K_{DP}^{0.634} Z^{0.258}$ if $\sigma = 15°$, $b/a = 0.6$, and $\lambda = 110.8$ mm, which is close to the theoretical relation, (17), $\sigma_{et} = 8.7 K_{DP}^{0.72} Z^{0.28}$.

Similarly, the expression for visibility with $\varepsilon = 0.05$ (5%) threshold becomes

$$\mathrm{Vis}(K_{DP}, Z) = 21.44 \times (F_o F_s)^{0.634} (K_{DP}\lambda)^{-0.634} Z^{-0.258}, \quad (21)$$

whereas if $\varepsilon = 0.02$ (2%) threshold is used,

$$\mathrm{Vis}(K_{DP}, Z) = 27.96 \times (F_o F_s)^{0.634} (K_{DP}\lambda)^{-0.634} Z^{-0.258}. \quad (22)$$

e. Sensitivity of empirical polarimetric relation for estimating σ_e

Bukovčić et al. (2018, 2020) demonstrated how the multipliers r_1 and r_2, and exponents p_1, p_2, q_1, and q_2, of the relations $S(K_{DP}, Z) = r_1 K_{DP}^{p_1} Z^{q_1}$ and $\mathrm{IWC}(K_{DP}, Z) = r_2 K_{DP}^{p_2} Z^{q_2}$ depend on particle density, aspect ratio, and σ. It is shown that the biggest uncertainty comes from the variability of σ and b/a, whereas the change in snow density is partially accounted for by the density adjustment [i.e., through the ratio of squares of the measured and prescribed empirical velocities in Eq. (7) of Bukovčić et al. (2018)]. The situation is somewhat different with $\sigma_e(K_{DP}, Z)$, as it is more sensitive to changes in snow density than the $S(K_{DP}, Z)$ and $\mathrm{IWC}(K_{DP}, Z)$ relations due to the multiplication factor $1/f_{rim}^2$ in the theoretical relation multiplier [Eq. (16)]. A 20% increase (decrease) in snow density reduces (increases) the $\sigma_e(K_{DP}, Z) = \gamma K_{DP}^{\alpha} Z^{\beta}$ multiplier γ by 26% (46%), and the change in the relation's exponents α and β are ±1.3% and ±2%, respectively. However, the dependence of $\sigma_e(K_{DP}, Z)$ on the aspect ratio and σ is similar to the $S(K_{DP}, Z)$ and $\mathrm{IWC}(K_{DP}, Z)$ relations. The joint influence of σ and b/a (obtained from the 2DVD) on γ, α, and β is illustrated in Fig. 3.

As σ and b/a simultaneously increase, both α and β remain nearly constant. The largest change in α and β is 0.3% and 0.4% for $\sigma = 40°$ and an increase of b/a from 0.5 to 0.8, which implies that α and β can be regarded as practically invariant to changes in σ and b/a (Figs. 3a,b); note that $\alpha' = \alpha_1 f_{rim}$, where $\alpha_1 = 0.178$ and $\beta_1 = -0.922$ are multiplier and exponent of snow density relation, (6) (Brandes et al. 2007). In contrast, the multiplier γ shows a significantly different dependence on σ and b/a (Fig. 3c). For aspect ratios between 0.5 and 0.8 and a constant value of σ, γ can increase by a factor of 2.4. The increase in γ is ~3.6 times if σ and b/a simultaneously increase from 0° to 40° and from 0.5 to 0.7 (i.e., the range of characteristic values for aggregated snow; Korolev and Isaac 2003), which makes a tremendous difference in the $\sigma_e(K_{DP}, Z)$ estimates.

4. Validation of polarimetric radar estimates of σ_e: Case studies

We choose to present a comparison of σ_e estimates/measurements rather than visibility as the former is directly measured at ASOS sites; this avoids confusion regarding the value of ε and day versus night estimates. It is straightforward to obtain visibility via (1) and/or (3) for a particular application or comparison. Four events that had significant societal impacts are chosen for verification and are summarized in Table 2. The radar-estimated σ_e from CVP/EVP and RD-QVPs are extracted via (20) from 200 to 700 m altitude AGL using the aforementioned values of $b/a = 0.6$ and σ between 25° and 29° (depending on the depth below the DGL; in our approach σ linearly increases from 10° in the DGL to 30° at the ground—typical of aggregates). The choice of altitude (200, 350, and 700 m) is dictated by the quality of K_{DP} estimates at low levels (in RD-QVPs and CVPs, the altitude is determined as the level where the change in σ_e between adjacent levels is small). As an additional source of comparison, we utilize the $S(\sigma_e)$ relations from WG-69 (line 4 in Fig. 1a), and FJ-83 (line 8 in Fig. 1a) using the standard radar $Z(S) = 120S^2$ relation. Hence, the WG-69 relation becomes $\sigma_e(\text{WG-69}) = 2.54S(Z)$, and the FJ-83 relation is $\sigma_e(\text{FJ-83}) = 3.912S(Z)^{0.66}$.

a. 8 December 2013

The 8 December 2013 event was a high-impact storm formed via warm air advection over a stationary front, with low-level dry air in place across the region. During the event, a frontogenetically forced band of heavy snow formed across the

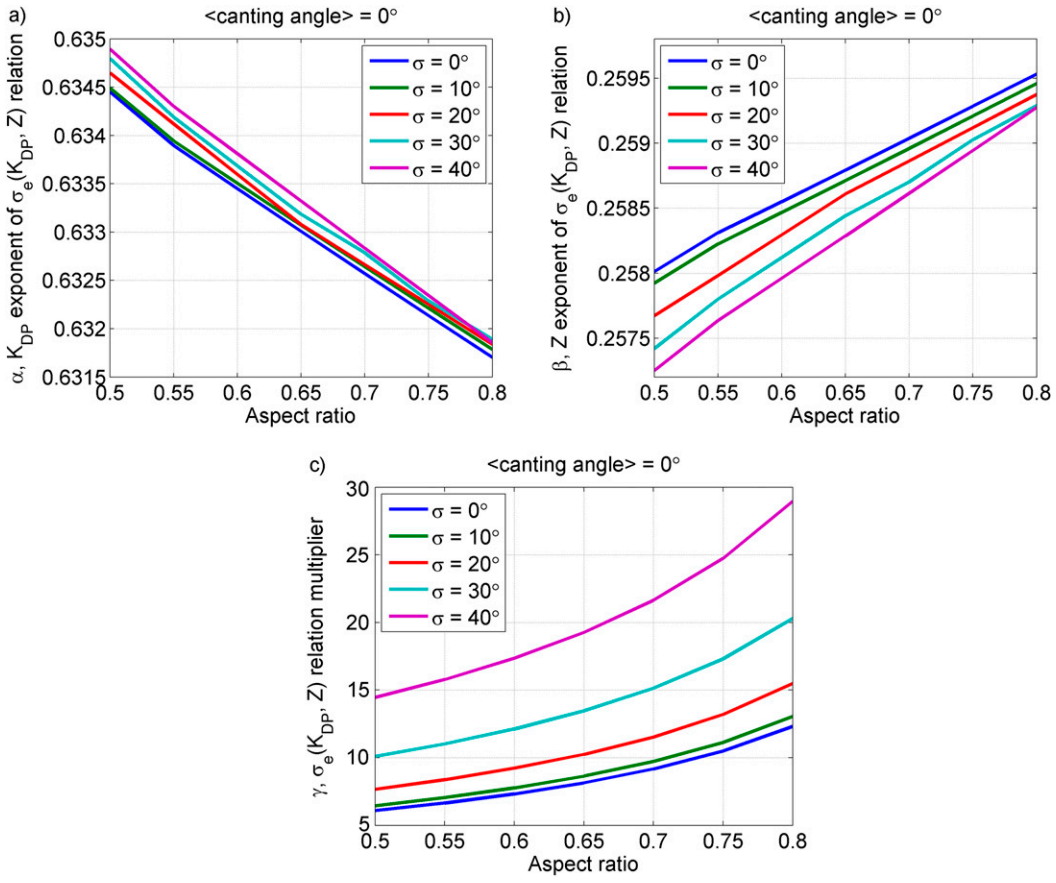

FIG. 3. Dependence of the $\sigma_e(K_{DP}, Z)$ relation's (a) K_{DP} exponent α, (b) Z exponent β, and (c) multiplier γ, on σ and b/a, computed from Oklahoma 2DVD measurements for zero-mean canting angle ($\langle$canting angle$\rangle = 0°$).

Philadelphia, Pennsylvania, metropolitan area and southern New Jersey. Several bridges were closed for hours, with multiple car accidents reported in the region. The nationally televised football game between the Philadelphia Eagles and Detroit Lions experienced so-called whiteout conditions, characterized by extremely low visibilities.

CVPs from KDIX of Z, K_{DP}, Z_{DR}, and ρ_{hv} constructed over KPNE ASOS station are presented in Fig. 4. The gaps at certain levels are dependent on the CVP radius size and radar volume coverage pattern (VCP) and exist because the data from corresponding elevations do not overlap; this is more pronounced at distances further from the radar. The temperature profile is extracted from RAP model analyses. The most noticeable feature in all variables is the absence of precipitation at lower altitudes until ~1600 UTC, caused by low-level dry air. It took about 4 h for the air to saturate and precipitation to start reaching the ground. The enhanced band of K_{DP} and Z_{DR} (with decreasing Z) in the sublimation layer early in the period is suggestive of a high concentration of anisotropic particles and may be due to secondary ice production. Several snowbands passed over KPNE, as seen from the reflectivity enhancements ($Z > 25$ dBZ) at ~1630, 1815, 2010, 2100, and 2230 UTC. The enhancements in K_{DP} (>0.15° km^{-1}) are usually within the DGL, where dendrites and/or plates experience rapid depositional growth. The Z_{DR} enhancements ($Z_{DR} >$ 0.6 dB) are also seen in the DGL. These higher values of K_{DP} and Z_{DR} in the DGL are due to the anisotropic shapes of crystals which have much higher densities than aggregated snowflakes. Besides, K_{DP} is proportional to particle concentration whereas Z_{DR} is not affected by the number of particles.

TABLE 2. Details of selected validation cases.

Date	Event type	Radar site (VCP)	Vertical profile type (radius in km)	ASOS site	Radar–ASOS distance (km)	Retrieval height (m AGL)
8 Dec 2013	Warm-air advection	KDIX (32, 21)	CVP (10)	KPNE	53.4	700
23 Jan 2016	Nor'easter	KLWX (21)	RD-QVP (15)	KIAD	5.7	350
14–15 Mar 2017	Nor'easter	KBGM (31, 21)	RD-QVP (15)	KBGM	0.9	350
18 Dec 2019	Snow squall	KOKX (32, 215)	EVP (3)	KISP	21.5	200

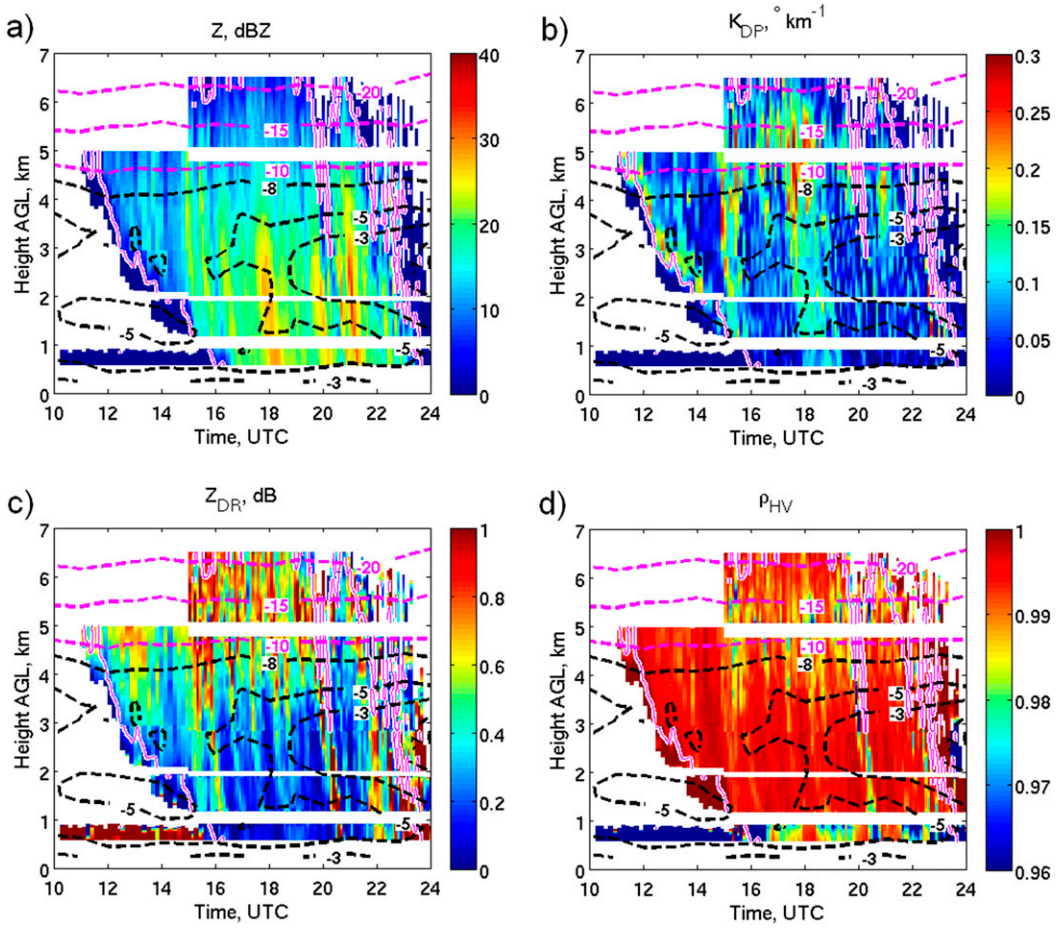

FIG. 4. CVPs of (a) Z, (b) K_{DP}, (c) Z_{DR}, and (d) ρ_{hv} obtained from KDIX scans (10 km radius) over the KPNE ASOS station ~54 km west of radar. The black dashed lines are isotherms from the RAP model analysis, where the DGL (between −10°C and −20°C) is highlighted in magenta; thin magenta lines within the thicker white lines represent a 10 dB SNR threshold; 8 Dec 2013, Philadelphia.

Adjacent to the ground, K_{DP} and Z_{DR} are very noisy and close to zero in heavily aggregated snow due to low particle densities and quasi-spherical shapes. During the main period of precipitation, the K_{DP} and Z appear to be well anticorrelated, with periods of more intense aggregation (higher Z, lower K_{DP}, and Z_{DR}) and less intense aggregation (lower Z, higher K_{DP}, and Z_{DR}; e.g., 1800 to 1930 UTC). These periods are not entirely distinct, though, and there are brief periods of overlap where it appears there is higher K_{DP} coincident with higher Z due to an enhanced number of small crystals. The ρ_{hv} field is mostly uniform and close to 1 with some reduction within the DGL due to the diversity of ice crystal shapes. The ρ_{hv} values near the ground appear to be artificially low due to CVP processing; sidelobe contamination from ground clutter may be included and affecting ρ_{hv} more than the other variables. The examination of a similar CVP above the nearby KPHL station (~20–25 km southwest of KPNE) does not show such features at 0.7 to 1 km AGL (not shown). Note that the low values of Z, K_{DP}, ρ_{hv}, and extremely high Z_{DR}, before 1600 UTC in the 0.7–1 km layer, are likely caused by low SNR (<10 dB).

Figure 5 shows a comparison of σ_e(WG-69), σ_e(FJ-83), and $\sigma_e(K_{DP}, Z)$ estimated from the CVP data at 700 m AGL and that measured at KPNE. Except for a few periods of minor/moderate discrepancies, the agreement between the $\sigma_e(K_{DP}, Z)$ estimates and the ASOS ground measurements is very good. In contrast, both σ_e(FJ-83) and σ_e(WG-69) show underestimation from 1745 to 1945 UTC and overestimation of σ_e from 1945 UTC until the end of the event. As shown in Fig. 4, there is a very dry air present above the ASOS location from 1200 to ~1600 UTC, hence we attribute the difference between the ASOS and all radar estimates from ~1550 to 1710 UTC to sublimation. This is because of the height difference between the ground (gauge) and radar estimates aloft (~700 m) and the time needed for the dry layer to saturate. Another period of larger discrepancies regarding $\sigma_e(K_{DP}, Z)$, from 2100 to 2200 UTC, is characterized by relatively large snowflakes, judging by the high Z values (~30 dBZ) and relatively low (~0.06° km^{-1}) K_{DP} (but higher than expected for Z ~ 30 dBZ). We speculate that these brief periods of overlap, where it appears there is

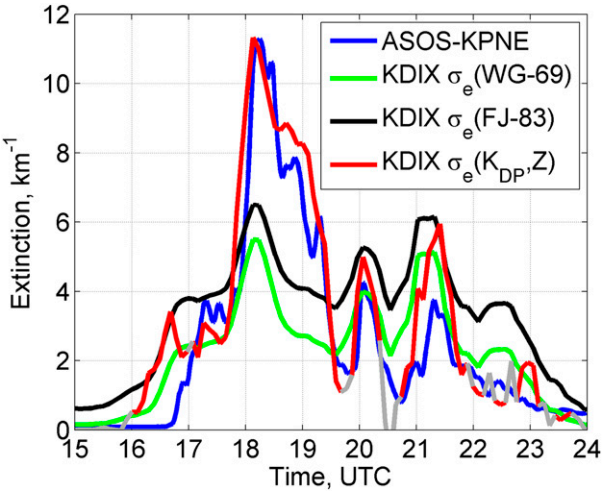

FIG. 5. The evolution of the extinction coefficient σ_e measured with the KPNE ASOS gauge (blue curve), and estimated from KDIX CVP: σ_e(WG-69) (green curve), σ_e(FJ-83) (black curve), and $\sigma_e(K_{DP}, Z)$ (red curve; silver curve indicates $K_{DP} < 0.01° km^{-1}$) at 700m AGL.

somewhat elevated K_{DP} alongside enhanced Z, are due to an enhanced number of small crystals.

Certain weather conditions, such as haze, mist, fog, and/or freezing fog, may affect the ground measurements of σ_e and/or the radar algorithm performance. The Meteorological Aerodrome Report (METAR) from KPNE reported snow with freezing fog from 1754 to 1854 UTC, followed by snow with mist from 1944 to 2254 UTC (last snow report), with mist continuing through 2354 UTC. Because of the ASOS fog/mist algorithm logic (see section 5), the mere inclusion of mist or fog accompanying precipitation in a METAR does not necessarily mean that the diminished visibility is appreciably due to mist or fog (and thus not likely to be reflected in the radar-based estimates of extinction coefficient/visibility).

b. 23 January 2016

The 23 January 2016 event was a classical nor'easter that tracked from the Gulf of Mexico to the New England coast and brought prolific snow totals to the entire northern mid-Atlantic region and widespread reports of visibilities ≤ 1/4 mi. This storm was categorized as the fourth most crippling northeast U.S. snowstorm since 1956 on the Northeast snowfall impact scale (NESIS; Kocin and Uccellini 2004) and was ranked as the sixth most impactful storm according to the regional snowfall index (RSI; Squires et al. 2014) affecting about 100 million people in total. Schools were closed for up to a week, widespread power outages occurred, and ~11 000 flights were canceled during and immediately after the storm.

The RD-QVPs (15-km radius) of Z, K_{DP}, Z_{DR}, and ρ_{hv}, obtained from the KLWX radar reveal the storm's evolution (Fig. 6). Numerous snowbands passed over the KIAD site during the storm, with the strongest ones (in terms of depth and Z) primarily between 0700 and 1100 UTC. The RD-QVPs of K_{DP} and Z_{DR} display rather interesting features in the DGL, where two dominant types of ice crystals, isometric (I type) and dendritic (D type), can be found (Griffin et al. 2018). I-type particles include a broad category of snow aggregates and ice crystals with nearly spherical or irregular shapes and can result in low to moderate Z_{DR} and significant K_{DP} if the concentration is sufficiently high. D-type crystals comprise highly oblate dendrites or hexagonal plates or prolate needles that have a higher density than I-type ice particles and are highly anisotropic in shape. These ice crystals can exhibit discernable K_{DP} (if their concentration is sufficiently high) and extremely large Z_{DR} regardless of concentration. Dendrites and hexagonal plates (needles) grow primarily between −10° and −20°C (−3° and −8°C), whereas I-type crystals can be generated throughout the full depth of the cloud. Hence, the regions of high Z_{DR} are dominated by D-type ice, and the high-K_{DP} regions are populated predominantly with I-type ice, although the existence of D-type ice is not precluded. As seen in the RD-QVP, the enhanced Z_{DR} values are especially well aligned with the −15°C isotherm, whereas the increased values of K_{DP} (up to $0.23° km^{-1}$) extend well below the DGL during multiple periods (usually marking the onset of efficient aggregation close to the ground). The most interesting K_{DP} signature is the well-defined streak slightly before 0800 UTC. The K_{DP} streak coincides with a column of enhanced Z and the highest cloud tops. Therefore, there is plenty of I-type snow in high concentration seeding the DGL (Griffin et al. 2018). Within the streak, K_{DP} decreases toward the surface, indicative of aggregation. However, not all ice particles aggregate, and a good fraction of high-density nonspherical particles (possibly due to riming) remain. Secondary ice production (SIP) due to rime splintering could also be at play in the region between 2 and 3 km from 0200 to 0400 UTC, with a lack of large particles resulting in lower Z and high Z_{DR} values due to small, anisotropic particles apparent. Temperatures in this region are between −8° and −3°C, a range favorable for the Hallett–Mossop process to be active. Also, these temperatures are favorable for the growth of highly anisotropic needles. Closer to the ground, the process of aggregation starts to dominate; as a consequence of the enlarged particle sizes, Z increases. At the same time that the particles' densities decrease, they become more spherical and/or chaotically oriented, hence K_{DP} and Z_{DR} approach zero near the ground. Although side-lobe contamination is likely affecting ρ_{hv} (appearing as horizontal streaks of decreased ρ_{hv} values), it is evident that D-type ice is correlated with a reduction in ρ_{hv} (and moderate to high Z_{DR}) whereas the (less oblate) aggregates have more uniform ρ_{hv} values closer to 1.

The evolution of σ_e(WG-69), σ_e(FJ-83), and $\sigma_e(K_{DP}, Z)$ estimated from the KLWX RD-QVP at 350 m AGL and measured by the collocated KIAD ASOS gauge is presented in Fig. 7. The comparison between the σ_e(WG-69), σ_e(FJ-83) and ASOS σ_e measurements show good agreement from 0000 to 0630 UTC and 2130 to 2330 UTC, whereas from 0630 until 2130 UTC both relations moderately underestimate the ASOS observations. The polarimetric $\sigma_e(K_{DP}, Z)$ relation and the ASOS ground measurement display excellent agreement from the beginning of the storm until ~1000 UTC, and from 1930 UTC until the end of the event, with a period of moderate

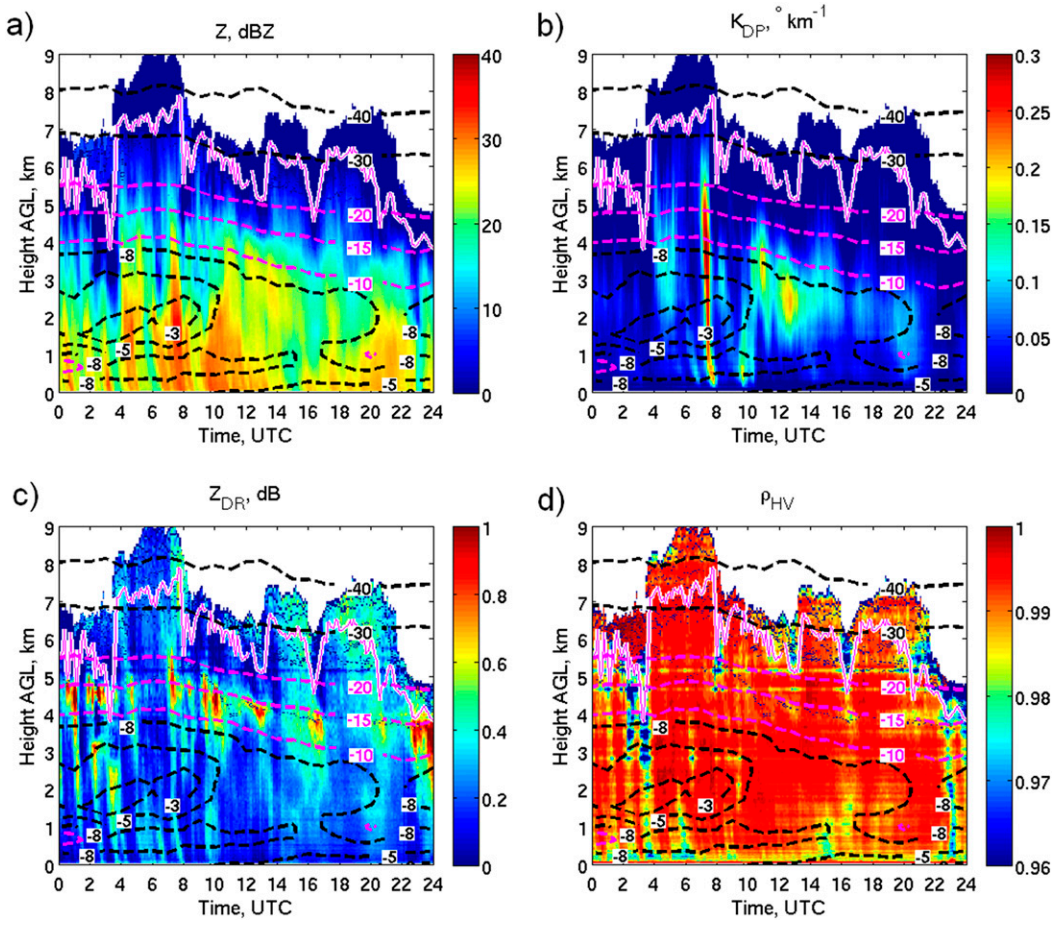

FIG. 6. RD-QVPs of (a) Z, (b) K_{DP}, (c) Z_{DR}, and (d) ρ_{hv} obtained from KLWX radar (15 km radius) collocated with the KIAD ASOS station. The black dashed lines are isotherms from the RAP model analysis, where the DGL (between −10°C and −20°C) is highlighted magenta; thin magenta lines within the thicker white lines represent a 10 dB SNR threshold; 23 Jan 2016, Sterling, Virginia.

to large discrepancies in between. METAR reports from KIAD show the presence of mist until 0500 UTC, freezing fog from 0500 to 1500 UTC, and blowing snow from 1500 to 2400 UTC. While there is a possibility that appreciable mist/fog and/or blowing snow concurrent with the snow could enhance σ_e beyond what the radar can observe from snow only (see section 5), this bias may be due to the strong winds present during precisely this period. Reports of strong winds (>8 m s^{-1}) exist from ~1000 to 2000 UTC, with the highest wind gust of 18 m s^{-1} at 1200 UTC, coincident with the largest discrepancy between $\sigma_e(K_{DP}, Z)$ and the ASOS measurements. RAP analysis wind profiles display a layer of strong winds (>30 m s^{-1}) between 1 and 2 km AGL from ~1100 to 1600 UTC (with speeds >25 m s^{-1} from 1000 to 2000 UTC), whereas the RD-QVP of spectrum width indicated a layer of enhanced wind shear/turbulence below 1.5 km AGL, coinciding temporally with the strong winds (not shown). While somewhat circumstantial, we submit that turbulence due to strong winds contributed to a decrease in radar $\sigma_e(K_{DP}, Z)$ by increasing σ beyond what was assumed, which in conjunction with blowing snow caused large discrepancies between the radar estimates and ground measurements.

c. 14–15 March 2017

Another high-impact storm chosen for analysis was a nor'easter that occurred on 14–15 March 2017. This storm ranked twenty-third on the NESIS scale and twelfth on the RSI scale, affecting over 60 million people and canceling over 8000 flights. The storm produced widespread heavy snow via several mesoscale snowbands throughout the interior mid-Atlantic and Northeast and brought hurricane-force wind gusts to coastal New England. Daily snowfall records were broken at several locations (e.g., Binghamton, New York; Scranton, Pennsylvania; Burlington, Vermont), with a maximum snowfall total of 42 in. (~107 cm) in West Winfield, New York.

RD-QVPs of Z, K_{DP}, Z_{DR}, and ρ_{hv}, constructed from KBGM radar and collocated with the KBGM ASOS station are presented in Fig. 8. The storm produced moderate to heavy precipitation from 0700 to 1500 UTC, followed by a few intense snowbands later in the event, revealed by the enhanced Z

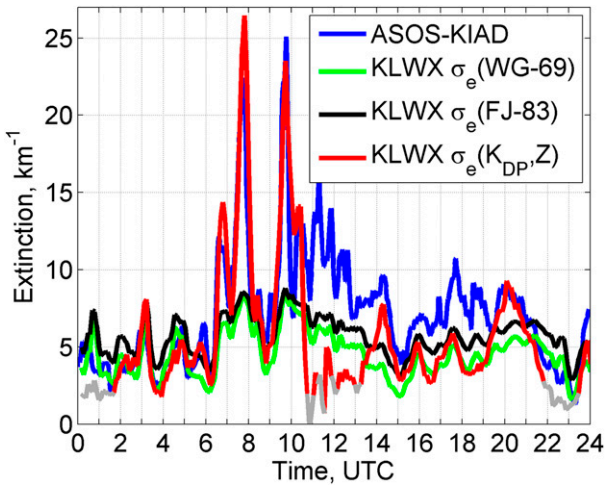

FIG. 7. The evolution of the extinction coefficient σ_e measured with the KIAD ASOS gauge (blue curve), and estimated from KLWX RD-QVP: σ_e(WG-69) (green curve), σ_e(FJ-83) (black curve), and $\sigma_e(K_{DP}, Z)$ (red curve; silver curve indicates $K_{DP} < 0.01^\circ\,km^{-1}$) at 350 m AGL.

values greater than 30 dBZ (Fig. 8a). Several interesting polarimetric signatures are revealed by K_{DP} and Z_{DR}. Increased values of Z_{DR} and K_{DP} in the DGL from 0700 to 1300 UTC extend almost to the ground, indicative of at least moderate concentrations of smaller and denser D-type crystals and a lower degree of aggregation at the ground. These may occasionally be mixed with I-type crystals, such as during the biggest K_{DP} enhancement aloft (~1100 UTC). Note that the biggest low-level enhancement in Z (~1215 UTC) coincides with the highest K_{DP} aloft (allowing for the time that snowflakes need to reach the ground). The cell at 1800 UTC is a mix of I-type and D-type crystals exposed by the high K_{DP}, moderately high Z_{DR}, and high Z values. After 1900 UTC, cloud-top heights and temperatures decrease, revealing D-type crystals that align well with the −15°C isotherm, with high Z_{DR} collocated with lower Z and low K_{DP}. This low concentration of pristine crystals that do not aggregate is seen as Z_{DR} streaks (~2010 and 2210 UTC) that reach almost to the ground. These signatures are in line with past observational studies (e.g., Williams et al. 2015; Griffin et al. 2018). The strange ρ_{hv} field is caused primarily by the usage of a less sensitive VCP 21 from 0500 to 2300 UTC (causing values lower than 0.96 aloft), as well as by sidelobe contamination. A change in VCP from 21 to 31 at 2215 UTC, which is a more sensitive mode of radar operation (another switch happened at ~0500 UTC from VCP 31 to 21), increases ρ_{hv} values aloft.

The comparison of σ_e(WG-69), σ_e(FJ-83), and $\sigma_e(K_{DP}, Z)$ obtained from 350 m AGL from the RD-QVP and σ_e measured at the KBGM ASOS site is presented in Fig. 9. Both σ_e(WG-69) and σ_e(FJ-83) result in moderate to large underestimations compared to the ASOS measurements throughout the event. In contrast, the shapes of the $\sigma_e(K_{DP}, Z)$ and ASOS curves show similarity in trend and good agreement, except for between 1200 and 1300 UTC and 2100 and 2330 UTC. The discrepancy in the latter period is most likely caused by strong winds, which exceed 7 m s^{-1} after 2000 UTC at KBGM. The discrepancy in the former period could be due to the localized nature of precipitation. The peak value of σ_e at ~1815 UTC is adequately reproduced with the polarimetric $\sigma_e(K_{DP}, Z)$ relation. It is worth mentioning that there was a brief report of mist when the snow started, followed by freezing fog lasting until 2131 UTC. Also, snow was not reported in the KBGM METAR between 1653 and 2131 UTC, and only snow was reported from 2153 UTC until the end of the event. We are skeptical about the lack of snow reports during this period given the reports of snow at nearby ASOS sites (KITH and KELM), a broad shield of moderate to heavy precipitation almost certainly not attributable solely to freezing fog (e.g., Z exceeding 30 dBZ at 1815 UTC), and quality-control flags that appear in the raw ASOS data during this period. Besides, high winds up to 16 m s^{-1} were recorded during this period and are known to potentially cause issues due to snow blocking the projector heads of the ASOS precipitation sensor (see ASOS manual, section 4.3.7).

d. 18 December 2019

As of 1 November 2018, NWS Weather Forecast Offices began issuing warnings for snow squalls. Snow squall warnings are issued "for intense but limited duration periods of moderate to heavy snowfall accompanied by gusty surface winds and resulting in greatly reduced visibilities and whiteout conditions" (NOAA 2019). One such event struck New York City on 18 December 2019. This fast-moving snow squall quickly enveloped the city, visually resembling a wall of snow. Although accumulations from snow squalls are usually small due to their short duration [e.g., KNYC reported just 0.4 in. (~1 cm) of snow], the intensity of snow, along with its rapid onset and attendant winds, created hazardous driving and overall conditions in the affected areas.

EVPs of Z, K_{DP}, Z_{DR}, and ρ_{hv} constructed from KOKX radar scans over the KISP are presented in Fig. 10. During the event, two cells passed over the ASOS site. The weaker, prefrontal cell was shallower and quite localized, lasting from 1900 to 2000 UTC. Relatively low Z values ($Z < 18$ dBZ), higher K_{DP} (up to ~0.2 °km^{-1}) and Z_{DR} (~0.4 dB), and a small reduction in ρ_{hv} within the precipitation core is indicative of a higher concentration of smaller, denser, and less aggregated particles occurring during the first cell. The stronger cell associated with the snow squall along the front passed quickly over KISP, lasting from 2200 to ~2240 UTC. The Z associated with the squall snow ranged between 25 and 30 dBZ, while K_{DP} values in the DGL reached 0.18° km^{-1} but were significantly reduced toward the ground. Z_{DR} was very low and close to zero where the Z values were high and vice versa, and ρ_{hv} was mostly uniform within the cell's core below the DGL, suggesting low-density aggregated snow with larger particles, in contrast to the first cell. Although the temperature aloft was similar between the two cells, more moisture was available during the squall, with relative humidity with respect to ice at the surface reaching 94% versus 78% during the first cell.

A comparison of the extinction coefficients σ_e measured at the KISP ASOS station and estimated from the KOKX EVP at 200 m AGL is presented in Fig. 11. $\sigma_e(K_{DP}, Z)$ and σ_e(FJ-83)

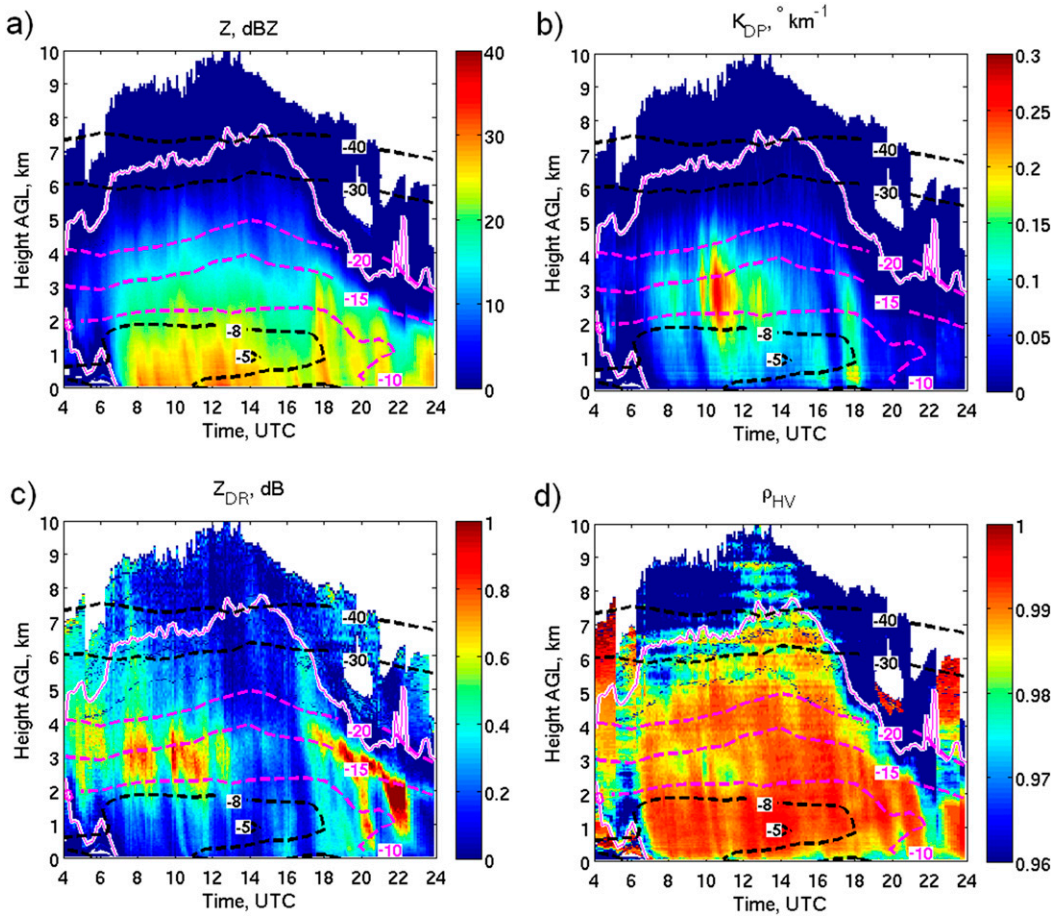

FIG. 8. RD-QVPs of (a) Z, (b) K_{DP}, (c) Z_{DR}, and (d) ρ_{hv} obtained from KBGM radar (15 km radius) collocated with the KBGM ASOS station. The black dashed lines are isotherms from the RAP model analyses, where the DGL (between −10° and −20°C) is highlighted magenta; thin magenta lines within the thicker white lines represent a 10 dB SNR threshold; 14 Mar 2017, Binghamton.

largely overestimate the ASOS KISP measurements during the weaker cell, whereas σ_e(WG-69) shows more consistent results. The assumed aspect ratio of 0.6 and σ of 28° used for the $\sigma_e(K_{DP}, Z)$ estimation are too high for snow with a low degree of aggregation, leading to a large overestimation. Smaller values of these parameters (0.5 and 5°–10°, respectively) in the $\sigma_e(K_{DP}, Z)$ retrieval produce comparable estimates with σ_e(WG-69) (not shown). The comparison is excellent for $\sigma_e(K_{DP}, Z)$ at the time of the squall snow cell passage, with the peaks in extinction coefficients in very good agreement; σ_e(FJ-83) shows moderate underestimation while σ_e(WG-69) shows even smaller values. Despite the short life span of this intense event (i.e., the squall snow), the polarimetric estimates of σ_e were able to adequately capture it, demonstrating the operational usefulness of this novel approach.

5. Discussion

The initial proof-of-concept results shown in section 4 are encouraging and deserve further exploration. Currently, the method requires spatial averaging in the form of RD-QVPs or CVPs/EVPs over a specific location to obtain the necessary high-quality estimates of K_{DP} in aggregated snow. If future methodologies are developed that offer high-quality, high-resolution estimates of K_{DP} in the horizontal, this approach offers the promise of spatially continuous estimates of σ_e/visibility as opposed to the relatively sparse point measurements currently available from ASOS stations. Such spatial fields may prove useful for the issuance of snow squall warnings.

An inevitable limitation of the proposed methodology is the lack of accounting for the below-beam effects. A frequent cause of changes to the SSD in the lowest levels is sublimation. This is particularly common at the start of many events, as cold and dry antecedent low-level polar air masses saturate in a top-down fashion from snow generated in the midlevels, as was the case for the 8 December 2013 event examined in section 4a. Due to the relatively low terminal velocity of snow, substantial mass loss due to sublimation can occur below the radar beam in relatively shallow depths close to the ground.

Idealized simulations using the one-dimensional snow model described in Carlin and Ryzhkov (2019) were conducted to

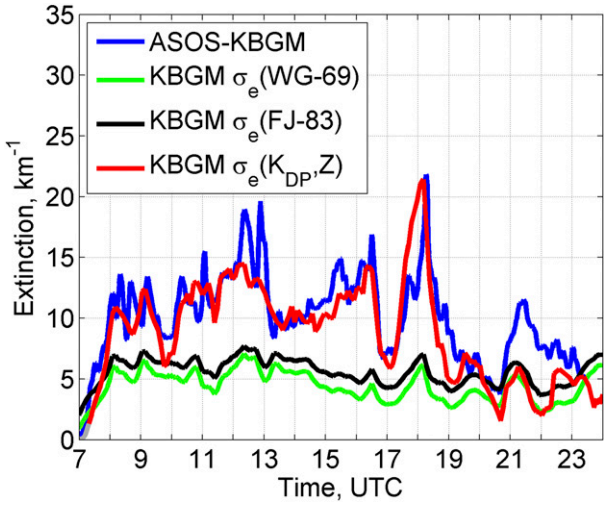

FIG. 9. The evolution of the extinction coefficient σ_e measured with the KBGM ASOS gauge (blue curve), and estimated from KBGMRD-QVP: σ_e(WG-69) (green curve), σ_e(FJ-83) (black curve), and $\sigma_e(K_{DP}, Z)$ (red curve; silver curve indicates $K_{DP} < 0.01^\circ\,km^{-1}$) at 350 m AGL.

simulate the change in the extinction coefficient over a 750-m depth (approximately the retrieval height for the 8 December 2013 case) for unrimed aggregates in a wide range of temperatures and relative humidities. The environment was assumed to be constant at all heights, and N_{0s} and Λ_s were assumed to be $3000\,m^{-3}\,mm^{-1}$ and $1.06\,mm^{-1}$, respectively, corresponding to an initial IWC of $\sim 0.5\,g\,m^{-3}$ and σ_e of $7.85\,km^{-1}$. For daytime visibility with a 5% threshold, this σ_e corresponds to the visibility of ~0.25 mi. The subsequent $\sigma_e s$ at the surface are shown in Fig. 12 as a fraction of the initial σ_e. For temperatures near 0°C, even a relative humidity (with respect to ice) of ~90% results in a 20% reduction of σ_e compared to 750 m, and for relative humidity <40% the reduction in σ_e exceeds 80%. These reductions correspond to daytime visibilities of ~0.30 and ~1.55 mi with the sensitivity to relative humidity slightly reduced at colder temperatures. If the air is dry enough through a large-enough depth, complete sublimation of snow can occur with no degradation in surface visibility observed at all.

Another obvious caveat of the proposed methodology in its current form is that it is formulated for aggregated snow. While severe reductions in visibility are often associated with heavy aggregated snow as opposed to pristine crystals, the application of the proposed equations to other habits requires modifying the relevant parameters—namely, α_1, β_1, d_1, and δ_1 in (6) and (7)—a priori.

Reductions in visibility during winter precipitation events may also occur due to conditions other than snow, including mist, fog, and/or freezing fog, and strong surface winds that cause blowing snow. However, the presence of mist and (freezing) fog are themselves inferred *from* the measured visibility and humidity at ASOS sites (e.g., if the dewpoint depression is approximately <2°C, fog is reported if the visibility is <5/8 mi, and mist is reported if the visibility is between 5/8 and 7 mi, irrespective of the observed precipitation type). Put another way, reductions in visibility due solely to snow can trigger reports of mist and fog, and as it does not take much snow to reduce visibilities below 7 mi, mist and fog reports frequently accompany snow reports. Indeed, the good results we observe at many periods during the cases examined coincident with reports of mist and fog support this interpretation. Of course, this does not preclude the fact that actual mist and fog can indeed reduce visibilities beyond that seen by the radar due to snow alone, and blowing snow near the surface remains a shortcoming of the method; both of these limitations will be inherent to all weather radar–based methods of estimating σ_e/visibility and would result in a universal underestimation of σ_e from the radar. In addition to blowing snow, strong surface winds can reduce K_{DP} by broadening the canting angle distribution, as was hypothesized to have occurred during a few of the cases examined. Estimates of σ_e from higher altitudes that may be less affected by strong turbulence could be used instead to mitigate this problem. While these polarimetric relations may apply all the way to the DGL, for practical applications the optimal height range for $\sigma_e(K_{DP}, Z)$ estimation is at heights closer to the ground.

Finally, due to (mostly spurious) negative values of K_{DP}, the algorithm can also result in negative $\sigma_e(K_{DP}, Z)$. The proposed remedy requires setting $\sigma_e(K_{DP}, Z)$ to zero for negative K_{DP} values, where only (infrequently occurring) prolate hydrometeors would be affected, as well as masking in regions where K_{DP} is smaller than a prescribed threshold (e.g., $K_{DP} < 0.01^\circ\,km^{-1}$, as indicated by the silver lines in Figs. 5, 7, 9, and 11) and may be less reliable. Another possibility involves replacing the less reliable $\sigma_e(K_{DP}, Z)$ values with ones estimated from previous studies if they are known to work better in given situations. Further investigation is needed to obtain more appropriate solutions to this shortcoming.

6. Summary

Historically, the NWS has used visibility (and/or extinction coefficient) to estimate snowfall rate intensity. Visibility–S (or σ_e–S) relations have been investigated in a large number of past studies and described through numerous power-law relations. However, Rasmussen et al. (1999) pointed out that the power-law relations between the visibility/extinction coefficient and snowfall rate are not sufficiently accurate due to natural variations of snow properties. In this study, we show that the extinction coefficient (equivalent to the second moment of the SSD) is a function of snowfall rate (i.e., a mass flux proportional to a somewhat higher SSD moment), as well as an inverse function of the f_{rim} and mean volume diameter [weakly dependent on the fall velocity exponent δ_1 in (7)]. Moreover, we show that the extinction coefficient is linearly related to the ice water content if an exponential SSD is assumed, depending on the multiplier α' (which accounts for variations in f_{rim}) of the snow density—equivolume diameter relation (6). The empirical data from this study confirmed these theoretical conclusions; the exponent in the empirical power-law relation between σ_e and IWC is 0.96 and hence very close to 1, while the σ_e–S exponent is 0.915. This is partly the reason why there is less scatter between σ_e and IWC compared to σ_e and S.

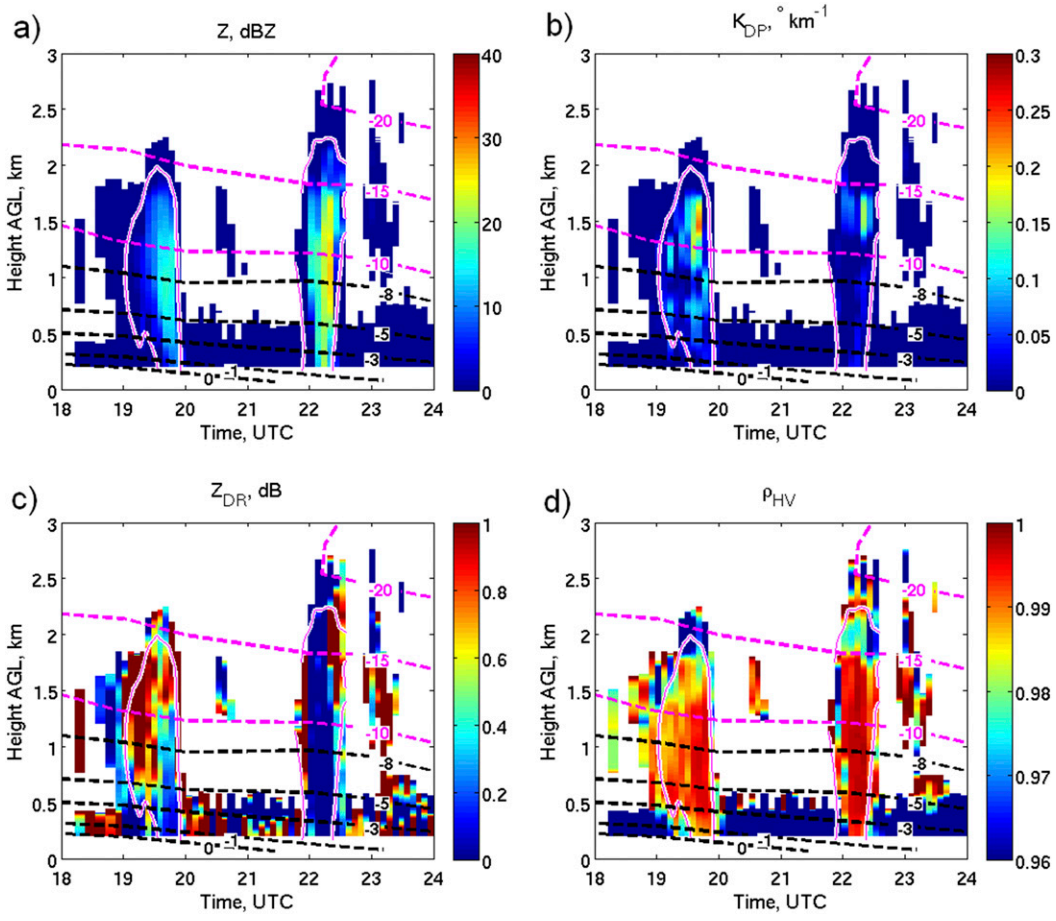

FIG. 10. EVPs of (a) Z, (b) K_{DP}, (c) Z_{DR}, and (d) ρ_{hv} obtained from KOKX scans (3 km radius) over the KISP ASOS station ~21 km west-southwest of radar. The black dashed lines are isotherms from the RAP model analyses, where the DGL (between −10° and −20°C) is shown in magenta; thin magenta lines within the thicker white lines represent a 10 dB SNR threshold; 18 Dec 2019, Upton, New York.

Previous studies were mainly centered on in situ measurements of the extinction coefficient (and visibility). An exception is a study by Muench and Brown (1977), who used Z to estimate the extinction coefficient (and visibility) but with only limited success. Our study is an attempt to extend estimations of the extinction coefficient and visibility beyond in situ measurements using polarimetric radar. A large set of 2DVD measurements from 16 Oklahoma snowstorms is used to obtain novel empirical polarimetric relations for the extinction coefficient and visibility from the combined use of K_{DP} and Z. Novel polarimetric relations $\sigma_e(K_{DP}, Z)$ and $\mathrm{Vis}(K_{DP}, Z)$ in the form of bivariate power laws are verified through comparison with theoretically derived relations and exhibit good agreement. Bukovčić et al. (2018, 2020) demonstrated that K_{DP} depends on particle density (i.e., degree of riming), aspect ratio, and particularly on the width of the canting angle distribution σ. These are the main reasons why the multiplier γ in the $\sigma_e(K_{DP}, Z)$ relation profoundly varies depending on these quantities, as demonstrated in sensitivity tests. In contrast, the relation's K_{DP} and Z exponents remain almost constant despite changes in aspect ratio and σ, although there is a slight change in both exponents (<2%) if the particle's density fluctuates ±20%. At the moment, the values of aspect ratio and σ used here are found in the existing literature and/or determined from empirical reasoning; future studies are needed to refine these estimates.

Comparisons between the ASOS ground measurements and polarimetric radar $\sigma_e(K_{DP}, Z)$ relation estimates and selected previous studies (WG-69; FJ-83) at various locations in the eastern United States produced realistic and encouraging results. The advantages of this novel approach are numerous as it is a remote sensing estimate of extinction coefficient/visibility versus a point source estimate (e.g., what is measured at ASOS sites). The use of such information could fill in the huge gaps that exist due to the sparse nature of in situ measurements in snowstorms. Moreover, the polarimetric nature of this estimate adds additional independent information, namely, vertically polarized radar returns. The combination of K_{DP} (proportional to the first moment of the snow size distribution and concentration in low-density snow) and Z (proportional to the fourth

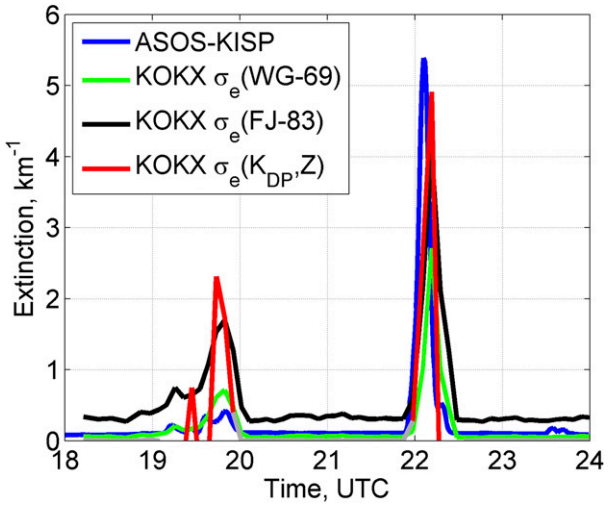

FIG. 11. The evolution of σ_e measured with the KISP ASOS gauge (blue curve), and estimated from KOKX EVP: σ_e(WG-69) (green curve), σ_e(FJ-83) (black curve), and $\sigma_e(K_{DP}, Z)$ (red curve; silver curve indicates $K_{DP} < 0.01°k\,km^{-1}$) at 200 m AGL.

moment of the snow size distribution in low-density snow) is very close to the second PSD moment, which what the intrinsic extinction coefficient is by definition. This reinforces our confidence in the pertinence of the proposed approach for polarimetric radar estimation of the extinction coefficient and visibility in aggregated snow. Additional visibility reductions due to blowing snow, (freezing) fog, and mist, as well as below-beam effects like sublimation, will not be reflected in radar-based estimates of the extinction coefficient; this needs to be considered in any practical application of such an approach.

The applicability of this novel approach also depends crucially on having reliable estimates of K_{DP}, which is low (at S band) and noisy in aggregated snow. The use of azimuthal (RD-QVPs) or localized (EVPs, CVPs) averaging generally improves the accuracy of K_{DP} and the reliability of the polarimetric relations. This approach should also be valid for C- and X-band radars (where K_{DP} values are higher due to their inverse dependence on the radar wavelength) for low-density snow aggregates up to 10–12 mm at X band and 16–20 mm at C band where the Rayleigh approximation applies (Bukovčić et al. 2020).

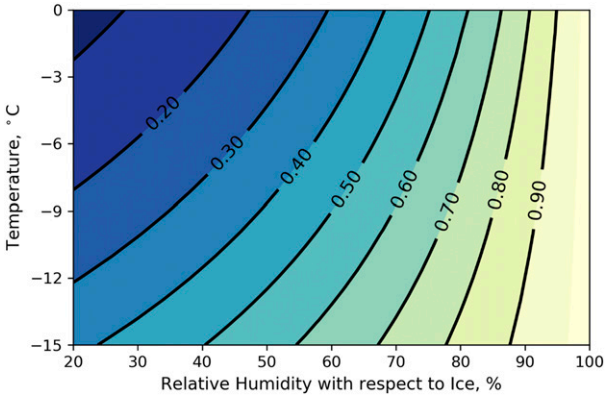

FIG. 12. Simulated reduction in extinction coefficient at the surface as a fraction of the initial value at 750 m for a wide range of relative humidities (with respect to ice) and temperatures using the one-dimensional snow model of Carlin and Ryzhkov (2019).

Acknowledgments. Special thanks are extended to John Krause for CVP and RD-QVP radar data processing and Dr. Guifu Zhang for the disdrometer data collection, as well as the three anonymous reviewers whose comments and suggestions greatly improved this manuscript. This work is supported by NOAA/Office of Oceanic and Atmospheric Research under NOAA–University of Oklahoma Cooperative Agreement NA16OAR4320115, U.S. Department of Commerce. Additional funding was provided through the NSF Grant 1841246.

APPENDIX

Derivations of Theoretical Relations

a. *Derivation of extinction coefficient relation from K_{DP} and Z*

Starting from the expression for the extinction coefficient σ_e (km^{-1}), defined as the second moment of the particle size distribution,

$$\sigma_e = \frac{\pi}{2} 10^{-3} \int_0^{D_{max}} D^2 N(D)\, dD, \tag{A1}$$

where D is snowflake equivolume diameter in mm, the integration yields

$$\sigma_e = \pi \times 10^{-3} N_{0s} \Lambda_s^{-3} \tag{A2}$$

for $N(D)$ ($m^{-3}\,mm^{-1}$) characterized by an exponential size distribution,

$$N(D) = N_{0s} \exp(-\Lambda_s D). \tag{A3}$$

Assuming the functional form

$$\sigma_{et} = \gamma_t K_{DP}^{\alpha_t} Z^{\beta_t}, \tag{A4}$$

an analytical relation between the σ_{et} and K_{DP}–Z can be obtained (herein subscript t stands for theoretical).

Under similar assumptions (see appendix in Bukovčić et al. 2020), it can also be shown that

$$Z = 0.224 \times \alpha_1^2 f_{rim}^2 N_{0s} \Lambda_s^{-(7+2\beta_1)} \Gamma(7 + 2\beta_1) \quad \text{and} \tag{A5}$$

$$K_{DP} = \frac{5.66 \times 10^{-2} \pi F_o F_s}{\lambda} \alpha_1^2 f_{rim}^2 N_{0s} \Lambda_s^{-(4+2\beta_1)} \Gamma(4 + 2\beta_1). \tag{A6}$$

Here Z is in $mm^6\,m^{-3}$, K_{DP} is in $°\,km^{-1}$, F_o and F_s are the orientation and shape factors (Ryzhkov et al. 2018; Ryzhkov and Zrnić 2019), and Γ is the complete gamma function. The density of aggregated snow ρ_s ($g\,cm^{-3}$) is inversely proportional to the particle equivolume diameter (mm) (Zawadzki et al. 2005; Brandes et al. 2007),

$$\rho_s(D) = \alpha' D^{\beta_1} = \alpha_1 f_{\rm rim} D^{\beta_1}, \tag{A7}$$

where β_1 is close to -1 and $\alpha_1 = 0.178$.

Substituting (A5), and (A6) into (A4), we obtain from N_{0s} exponents

$$\alpha_t = 1 - \beta_t, \tag{A8}$$

and from Λ_s exponents

$$\beta_t = -\frac{1+2\beta_1}{3} \quad \text{and} \quad \alpha_t = \frac{4+2\beta_1}{3}; \tag{A9}$$

hence,

$$\sigma_{et} = \gamma_t K_{\rm DP}^{(4+2\beta_1)/3} Z^{-(1+2\beta_1)/3}. \tag{A10}$$

Solving (A10) for γ_t from (A2), (A5), and (A6) provides the expression

$$\gamma_t = \frac{\pi \times 10^{-3} \times [0.224 \times \Gamma(7+2\beta_1)]^{(1+2\beta_1)/3}}{\alpha_1^2 f_{\rm rim}^2 \times \left[0.178 \times \frac{F_o F_s}{\lambda} \times \Gamma(4+2\beta_1)\right]^{(4+2\beta_1)/3}}. \tag{A11}$$

b. The dependence of the extinction coefficient on S

Starting from the expression for σ_{et} (A10), and S [mm h^{-1}, see (A13) in Bukovčić et al. 2020],

$$S = c_s K_{\rm DP}^{(3+\beta_1-\delta_1)/3} Z^{(-\beta_1+\delta_1)/3}, \tag{A12}$$

the ratio between them is

$$\frac{\sigma_{\rm et}}{S} = \frac{\gamma_t K_{\rm DP}^{(4+2\beta_1)/3} Z^{-(1+2\beta_1)/3}}{c_s K_{\rm DP}^{(3+\beta_1-\delta_1)/3} Z^{(-\beta_1+\delta_1)/3}} = \frac{\gamma_t}{c_s} \left(\frac{K_{\rm DP}}{Z}\right)^{(1+\beta_1+\delta_1)/3}, \tag{A13}$$

where

$$c_s = \frac{10.61 \times 10^{-3} \times d_1 \times f(\rho_a) \times \Gamma(4+\beta_1+\delta_1)}{\alpha_1 f_{\rm rim} \times \left[\frac{F_o F_s}{\lambda} \times \Gamma(4+2\beta_1)\right]^{(3+\beta_1-\delta_1)/3} \times [1.26 \times \Gamma(7+2\beta_1)]^{(\delta_1-\beta_1)/3}}. \tag{A14}$$

The term $d_1 f(\rho_a)$ in (A14) originates from the snowflake terminal velocity relation V_t, which is a weak function of particle diameter D ($\delta_1 \approx 0.15$, see appendix in Bukovčić et al. 2020),

$$V_t(D) = d_1 f(\rho_a) D^{\delta_1}, \tag{A15}$$

and $f(\rho_a)$ is a function of atmospheric density and/or pressure.

It follows from (A5) and (A6) that

$$\frac{K_{\rm DP}}{Z} = 0.79 \frac{F_o F_s}{\lambda} \Lambda_s^3 \frac{\Gamma(4+2\beta_1)}{\Gamma(7+2\beta_1)}. \tag{A16}$$

Substituting (A11), (A14), and (A16) in (A13), and using $\Lambda_S = 4/D_m$ valid for the exponential SSD (A3), the theoretical relation between the $\sigma_{\rm et}$ and S is derived in the form

$$\sigma_{et} = \frac{6.66 \times 4^{\beta_1+\delta_1}}{\alpha_1 f_{\rm rim} d_1 f(\rho_a) \Gamma(4+\beta_1+\delta_1) D_m^{1+\beta_1+\delta_1}} S. \tag{A17}$$

c. The dependence of the extinction coefficient on IWC

Starting from the expression for σ_e (A2), and IWC [g m^{-3}, see (A15) and (A16) in Bukovčić et al. 2020],

$$\text{IWC} = \frac{\pi}{6} 10^{-3} \alpha_1 f_{\rm rim} N_{0s} \Lambda_s^{-(4+\beta_1)} \Gamma(4+\beta_1), \tag{A18}$$

and assuming a functional form

$$\sigma_e = a_e \text{IWC}^{b_e}, \tag{A19}$$

$$\pi \times 10^{-3} N_{0s} \Lambda_s^{-3} = a_e \left[\frac{\pi}{6} 10^{-3} \alpha_1 f_{\rm rim} N_{0s} \Lambda_s^{-(4+\beta_1)} \Gamma(4+\beta_1)\right]^{b_e}.$$

It follows from the N_{0s} exponents that $b_e = 1$.

Under the same assumptions as for (A7), $\beta_1 \approx -1$, one can obtain the expression

$$a_e = \frac{3}{\alpha_1 f_{\rm rim}} \quad \text{and} \tag{A20}$$

$$\sigma_e = \frac{3}{\alpha_1 f_{\rm rim}} \text{IWC}. \tag{A21}$$

REFERENCES

Allabakash, S., S. Lim, V. Chandrasekar, K. H. Min, J. Choi, and B. Jang, 2019: X-band dual-polarization radar observations of snow growth processes of a severe winter storm: Case of 12 December 2013 in South Korea. *J. Atmos. Oceanic Technol.*, **36**, 1217–1235, https://doi.org/10.1175/JTECH-D-18-0076.1.

Allard, E., 1876: *Mémorie sur l'Intensiteet la Porteé des Phares.* Dunod, 70 pp.

Aydin, K., and C. Tang, 1995: Estimation of ice water content with 94-GHz millimeter wave radar observables. Preprints, *27th Conf. on Radar Meteorology*, Vail, CO, Amer. Meteor. Soc., 550–552.

Benjamin, S. G., G. A. Grell, J. M. Brown, T. G. Smirnova, and R. Black, 2004: Mesoscale weather prediction with the RUC hybrid isentropic–terrain-following coordinate model. *Mon. Wea. Rev.*, **132**, 473–494, https://doi.org/10.1175/1520-0493(2004)132<0473:MWPWTR>2.0.CO;2.

Bisyarin, V. P., I. P. Bisyarina, V. K. Rubash, and A. K. Sokolov, 1971: Attenuation of 10.6 and 0.63 mm laser radiation in atmospheric precipitation. *Radio Eng. Electron. Phys.*, **16**, 1594–1597.

Black, A. W., and T. L. Mote, 2015: Characteristics of winter-precipitation-related transportation fatalities in the United States. *Wea. Climate Soc.*, **7**, 133–145, https://doi.org/10.1175/WCAS-D-14-00011.1.

Boudala, F. S., and G. A. Isaac, 2009: Parameterization of visibility in snow: Application in numerical weather prediction models. *J. Geophys. Res.*, **114**, D19202, https://doi.org/10.1029/2008JD011130.

——, ——, R. W. Crawford, and J. Reid, 2012: Parameterization of runway visual range as a function of visibility: Implications for numerical weather prediction models. *J. Atmos. Oceanic Technol.*, **29**, 177–191, https://doi.org/10.1175/JTECH-D-11-00021.1.

Brandes, E. A., K. Ikeda, G. Zhang, M. Schönhuber, and R. M. Rasmussen, 2007: A statistical and physical description of hydrometeor distributions in Colorado snowstorms using a video disdrometer. *J. Appl. Meteor. Climatol.*, **46**, 634–650, https://doi.org/10.1175/JAM2489.1.

Bukovčić, P., 2017: Polarimetric measurements of ice pellets and aggregated snow. Ph.D. dissertation, University of Oklahoma, 120 pp., https://hdl.handle.net/11244/52406.

——, D. Zrnić, and G. Zhang, 2017: Winter precipitation liquid–ice phase transitions revealed with polarimetric radar and 2DVD observations in central Oklahoma. *J. Appl. Meteor. Climatol.*, **56**, 1345–1363, https://doi.org/10.1175/JAMC-D-16-0239.1.

——, A. Ryzhkov, D. Zrnić, and G. Zhang, 2018: Polarimetric radar relations for quantification of snow based on disdrometer data. *J. Appl. Meteor. Climatol.*, **57**, 103–120, https://doi.org/10.1175/JAMC-D-17-0090.1.

——, ——, and ——, 2020: Polarimetric relations for snow estimation—Radar verification. *J. Appl. Meteor. Climatol.*, **59**, 991–1009, https://doi.org/10.1175/JAMC-D-19-0140.1.

Capozzi, V., M. Montopoli, A. Bracci, E. Adirosi, L. Baldini, G. Vulpiani, and G. Budillon, 2020: Retrieval of snow precipitation rate from polarimetric X-band radar measurements in southern Italy Apennine mountains. *Atmos. Res.*, **236**, 104796, https://doi.org/10.1016/j.atmosres.2019.104796.

Carlin, J. T., and A. V. Ryzhkov, 2019: Estimation of melting-layer cooling rate from dual-polarization radar: Spectral bin model simulations. *J. Appl. Meteor. Climatol.*, **58**, 1485–1508, https://doi.org/10.1175/JAMC-D-18-0343.1.

Field, P. R., and A. J. Heymsfield, 2003: Aggregation and scaling of ice crystal size distributions. *J. Atmos. Sci.*, **60**, 544–560, https://doi.org/10.1175/1520-0469(2003)060<0544:AASOIC>2.0.CO;2.

Fujiyoshi, Y., G. Wakahamam, T. Endoh, S. Irikawa, H. Konishi, and M. Takeuchi, 1983: Simultaneous observation of snowfall intensity and visibility in winter at Sapporo. *Low Temp. Sci*, **42A**, 147–156.

Garrett, T. J., S. E. Yuter, C. Fallgatter, K. Shkurko, S. R. Rhodes, and J. L. Endries, 2015: Orientations and aspect ratios of falling snow. *Geophys. Res. Lett.*, **42**, 4617–4622, https://doi.org/10.1002/2015GL064040.

Griffin, E., T. Schuur, and A. Ryzhkov, 2018: A polarimetric analysis of ice microphysical processes in snow, using quasi-vertical profiles. *J. Appl. Meteor. Climatol.*, **57**, 31–50, https://doi.org/10.1175/JAMC-D-17-0033.1.

Gultepe, I., J. Milbrandt, and B.-B. Zhou, 2010: Visibility parameterization for forecasting model applications. *Fifth Int. Conf. on Fog, Fog Collection and Dew*, Münster, Germany, IFDA, 227–230, https://meetingorganizer.copernicus.org/FOGDEW2010/FOGDEW2010-112.pdf.

Gunn, K. L. S., and J. S. Marshall, 1958: The distribution with size of aggregate snowflakes. *J. Meteor.*, **15**, 452–461, https://doi.org/10.1175/1520-0469(1958)015<0452:TDWSOA>2.0.CO;2.

Hanesch, M., 1999: Fall velocity and shape of snowflakes. Ph.D. thesis, Swiss Federal Institute of Technology, 123 pp., http://ecollection.library.ethz.ch/eserv/eth:23207/eth-23207-02.pdf.

Hassan, D., P. A. Taylor, and G. A. Isaac, 2017: Snowfall rate estimation using C-band polarimetric radars. *Meteor. Appl.*, **24**, 142–156, https://doi.org/10.1002/met.1613.

Hendry, A., Y. Antar, and G. McCormick, 1987: On the relationship between the degree of preferred orientation in precipitation and dual-polarization radar echo characteristics. *Radio Sci.*, **22**, 37–50, https://doi.org/10.1029/RS022i001p00037.

Hogan, R. J., L. Tian, P. R. A. Brown, C. D. Westbrook, A. J. Heymsfield, and J. D. Eastment, 2012: Radar scattering from ice aggregates using the horizontally aligned oblate spheroid approximation. *J. Appl. Meteor. Climatol.*, **51**, 655–671, https://doi.org/10.1175/JAMC-D-11-074.1.

Huang, G.-J., V. N. Bringi, R. Cifelli, D. Hudak, and W. A. Petersen, 2010: A methodology to derive radar reflectivity–liquid equivalent snow rate relations using C-band radar and a 2D video disdrometer. *J. Atmos. Oceanic Technol.*, **27**, 637–651, https://doi.org/10.1175/2009JTECHA1284.1.

——, ——, D. Moisseev, W. A. Petersen, L. Bliven, and D. Hudak, 2015: Use of 2D-video disdrometer to derive mean density–size and Z_e–SR relations: Four snow cases from the light precipitation validation experiment. *Atmos. Res.*, **153**, 34–48, https://doi.org/10.1016/j.atmosres.2014.07.013.

Interagency Council on Advancing Meteorological Services, 2017: Surface weather observations and reports. OFCM Federal Meteorological Handbook 1, 98 pp.

Kocin, P. J., and L. W. Uccellini, 2004: A snowfall impact scale derived from Northeast storm snowfall distributions. *Bull. Amer. Meteor. Soc.*, **85**, 177–194, https://doi.org/10.1175/BAMS-85-2-Kocin.

Korolev, A., and G. Isaac, 2003: Roundness and aspect ratio of particles in ice clouds. *J. Atmos. Sci.*, **60**, 1795–1808, https://doi.org/10.1175/1520-0469(2003)060<1795:RAARAOP>2.0.CO;2.

Koschmieder, H. 1924: Theorie der horizontalen Sechtweite (Theory of horizontal visibility). *Beitr. Phys. Freien Atmos.*, **12**, 33–53.

Kruger, A., and W. F. Krajewski, 2002: Two-dimensional video disdrometer: A description. *J. Atmos. Oceanic Technol.*, **19**, 602–617, https://doi.org/10.1175/1520-0426(2002)019<0602:TDVDAD>2.0.CO;2.

Lillesæter, O., 1965: Parallel-beam attenuation of light, particularly by falling snow. *J. Appl. Meteor.*, **4**, 607–613, https://doi.org/10.1175/1520-0450(1965)004<0607:PBAOLP>2.0.CO;2.

Lo, K. K., and R. E. Passarelli Jr., 1982: Growth of snow in winter storms: An airborne observational study. *J. Atmos. Sci.*, **39**, 697–706, https://doi.org/10.1175/1520-0469(1982)039<0697:TGOSIW>2.0.CO;2.

Lu, Y., K. Aydin, E. Cothiaux, and J. Verlinde, 2015: Retrieving cloud ice water content using millimeter- and centimeter wavelength radar polarimetric observables. *J. Appl. Meteor. Climatol.*, **54**, 596–604, https://doi.org/10.1175/JAMC-D-14-0169.1.

Matrosov, S., and A. Heymsfield, 2017: Empirical relations between size parameters of ice hydrometeor populations and radar reflectivity. *J. Appl. Meteor. Climatol.*, **56**, 2479–2488, https://doi.org/10.1175/JAMC-D-17-0076.1.

——, R. Reinking, and I. Djalalova, 2005a: Inferring fall attitudes of pristine dendritic crystals from polarimetric radar data. *J. Atmos. Sci.*, **62**, 241–250, https://doi.org/10.1175/JAS-3356.1.

——, A. J. Heymsfield, and Z. Wang, 2005b: Dual-frequency radar ratio of nonspherical atmospheric hydrometeors. *Geophys. Res. Lett.*, **32**, L13816, https://doi.org/10.1029/2005GL023210.

Mellor, M., 1966: Light scattering and particle aggregation in snow storms. *J. Glaciol.*, **6**, 237–248, https://doi.org/10.1017/S0022143000019250.

Melnikov, V., and J. Straka, 2013: Axis ratios and flutter angles of cloud ice particles: Retrievals from radar data. *J. Atmos. Oceanic Technol.*, **30**, 1691–1703, https://doi.org/10.1175/JTECH-D-12-00212.1.

Mitchell, D. L., R. Zhang, and R. Pitter, 1990: Mass-dimensional relationship for ice particles and the influence of riming on snowfall rates. *J. Appl. Meteor.*, **29**, 153–163, https://doi.org/10.1175/1520-0450(1990)029<0153:MDRFIP>2.0.CO;2.

Muench, H., and H. Brown, 1977: Measurements of visibility and radar reflectivity during snowstorms in the AFGL Mesonet. NASA STI/Recon Tech. Rep. 78, 34 pp.

Murphy, A., A. Ryzhkov, and P. Zhang, 2020: Columnar vertical profile (CVP) methodology for validating polarimetric radar retrievals in ice using in situ aircraft measurements. *J. Atmos. Oceanic Technol.*, **37**, 1623–1642, https://doi.org/10.1175/JTECH-D-20-0011.1.

Nguyen, C. M., M. Wolde, K. Baibakov, and A. Korolev, 2017: Determination and estimation of high ice water content using X-band and W-band dual-polarization airborne radar data.*38th Conf. on Radar Meteorology*, Chicago, IL, Amer. Meteor. Soc., 89, https://ams.confex.com/ams/38RADAR/webprogram/Paper321101.html.

——, ——, and A. Korolev, 2019: Determination of ice water content (IWC) in tropical convective clouds from X-band dual-polarization airborne radar. *Atmos. Meas. Tech.*, **12**, 5897–5911, https://doi.org/10.5194/amt-12-5897-2019.

NOAA, 2019: Snow squall warning service update for winter season 2019-2020. NOAA Doc., 2 pp., https://www.weather.gov/media/nwr/Snow%20Squall_WRN_110519.pdf.

NWS, 1998: Automated Surface Observing System (ASOS) user's guide. NOAA Doc., 61 pp.

O'Brien, H. W., 1970: Visibility and light attenuation in falling snow. *J. Appl. Meteor.*, **9**, 671–683, https://doi.org/10.1175/1520-0450(1970)009<0671:VALAIF>2.0.CO;2.

Poljakova, E. A., and V. D. Tretjakov, 1960: Visibility in falling snow. *Gl. Geofiz. Obs.*, **100**, 53–57.

Rasmussen, R. M., J. Vivekanandan, J. Cole, B. Myers, and C. Masters, 1999: The estimation of snowfall rate using visibility. *J. Appl. Meteor.*, **38**, 1542–1563, https://doi.org/10.1175/1520-0450(1999)038<1542:TEOSRU>2.0.CO;2.

Ryzhkov, A., and D. Zrnić, 1998: Discrimination between rain and snow with a polarimetric radar. *J. Appl. Meteor.*, **37**, 1228–1240, https://doi.org/10.1175/1520-0450(1998)037<1228:DBRASW>2.0.CO;2.

——, and ——, 2019: *Radar Polarimetry for Weather Observations*. Springer International Publishing, 486 pp., https://doi.org/10.1007/978-3-030-05093-1.

——, P. Zhang, H. Reeves, M. Kumjian, T. Tschallener, S. Trömel, and C. Simmer, 2016: Quasi-vertical profiles—A new way to look at polarimetric radar data. *J. Atmos. Oceanic Technol.*, 33, 551–562, https://doi.org/10.1175/JTECH-D-15-0020.1.

——, P. Bukovčić, A. Murphy, P. Zhang, and G. McFarquhar, 2018: Ice microphysical retrievals using polarimetric radar data. *10th European Conf. on Radar in Meteorology and Hydrology*, Netherlands, KNMI, 40, https://projects.knmi.nl/erad2018/ERAD2018_extended_abstract_040.pdf.

Schönhuber, M., G. Lammer, and W. L. Randeu, 2008: The 2D-video-disdrometer. *Precipitation: Advances in Measurement, Estimation and Prediction*, S. Michaelides, Ed., Springer, 3–31.

Sekhon, R. S., and R. C. Srivastava, 1970: Snow size spectra and radar reflectivity. *J. Atmos. Sci.*, **27**, 299–307, https://doi.org/10.1175/1520-0469(1970)027<0299:SSSARR>2.0.CO;2.

Squires, M. F., J. H. Lawrimore, R. R. Heim Jr., D. A. Robinson, M. R. Gerbush, and T. W. Estilow, 2014: The regional snowfall index. *Bull. Amer. Meteor. Soc.*, **95**, 1835–1848, https://doi.org/10.1175/BAMS-D-13-00101.1.

Stallabrass, J. R., 1985: Measurements of the concentration of falling snow. *Snow Property Measurements Workshop*, Lake Louise, AB, Canada, National Research Council Canada, 389–410.

Stoelinga, M. T., and T. T. Warner, 1999: Nonhydrostatic, mesobeta-scale model simulations of cloud ceiling and visibility for an East Coast winter precipitation event. *J. Appl. Meteor.*, **38**, 385–404, https://doi.org/10.1175/1520-0450(1999)038<0385:NMSMSO>2.0.CO;2.

Tobin, D. M., and M. R. Kumjian, 2017: Polarimetric radar and surface-based precipitation-type observations of ice pellet to freezing rain transitions. *Wea. Forecasting*, **32**, 2065–2082, https://doi.org/10.1175/WAF-D-17-0054.1.

Vivekanandan, J., V. N. Bringi, M. Hagen, and P. Meischner, 1994: Polarimetric radar studies of atmospheric ice particles. *IEEE Trans. Geosci. Remote Sens.*, **32**, 1–10, https://doi.org/10.1109/36.285183.

Warner, C., and K. L. S. Gunn, 1969: Measurement of snowfall by optical attenuation. *J. Appl. Meteor.*, **8**, 110–121, https://doi.org/10.1175/1520-0450(1969)008<0110:MOSBOA>2.0.CO;2.

Williams, E., and Coauthors, 2015: Measurements of differential reflectivity in snowstorms and warm season stratiform systems. *J. Appl. Meteor. Climatol.*, **54**, 573–595, https://doi.org/10.1175/JAMC-D-14-0020.1.

World Meteorological Organization, 2003: Manual on the Global Observing System. WMO Rep. 544, 50 pp., https://www.wmo.int/pages/prog/www/OSY/Manual/WMO544.pdf.

——, 2008: Guide to meteorological instruments and methods of observation. 7th ed. WMO Rep. 8, 716 pp., http://library.wmo.int/pmb_ged/wmo_8_en-2012.pdf.

Zawadzki, I., W. Szyrmer, C. Bell, and F. Fabry, 2005: Modeling of the melting layer. Part III: The density effect. *J. Atmos. Sci.*, **62**, 3705–3723, https://doi.org/10.1175/JAS3563.1.

Zhang, G., 2016: *Weather Radar Polarimetry*. CRC Press, 304 pp.